Simple unilateral rupture of the great M_W 8.8 2025 Kamchatka earthquake

Chengli Liu, Yefei Bai, Thorne Lay, Ping He, Yangmao Wen, Xiong Xiong, and Tuncay Taymaz

Science **391** (6787), . DOI: 10.1126/science.aeb8232

Editor's summary

In late July 2025, a moment magnitude 8.8 earthquake struck off the Kamchatka Peninsula coast in Russia, sparking a trans-Pacific tsunami and triggering volcanic activity in the region. The event highlighted how the recurrence of great earthquakes may not follow regular patterns. Liu *et al.* combined teleseismic and satellite data with deep-water tsunami recordings to estimate the slip history for the 2025 event. Peak slip was greater than for the similarly located 1952 earthquake despite generating a weaker tsunami. Variable recurrence and slip distributions in this region suggest complex strain release patterns that may heighten seismic risk. —Angela Hessler

EARTHQUAKES

Simple unilateral rupture of the great M_w 8.8 2025 Kamchatka earthquake

Chengli Liu[1,2]*, Yefei Bai[3,4,5]*, Thorne Lay[6], Ping He[1], Yangmao Wen[7], Xiong Xiong[1,2], Tuncay Taymaz[8,9]

On 29 July 2025, a moment magnitude (M_w) 8.8 great earthquake ruptured along offshore southern Kamchatka, with the aftershock region overlapping that of a 1952 M_w 8.8 to 9.0 event. Like 1952, the 2025 event nucleated at the northeastern end of the rupture, preceded by intense foreshock activity. Joint inversion of teleseismic and InSAR (Interferometric Synthetic Aperture Radar) data for the space-time slip distribution, with validation by means of forward modeling of deep-water tsunami recordings, revealed a southwestward elongated large-slip patch on the curved plate boundary. A slip of up to 14 meters was located offshore southern Kamchatka and Paramushir Island. The 1952 earthquake generated stronger tsunami signals in Hawaii, indicating a different slip distribution. Peak slip in 2025 exceeded the maximum slip deficit accumulated since 1952. Observations of volcanic eruptions after multiple great earthquakes in Kamchatka provide compelling evidence of earthquake-volcano interactions.

The Kuril-Kamchatka subduction zone, which is characterized by a wide seismogenic zone (*1*, *2*) where the Pacific Plate and the Okhotsk microplate converge at ~8 cm/year (*3*), is recognized as one of the most seismically active regions worldwide (*4*–*8*). Kamchatka has experienced numerous great megathrust earthquakes, including events in 1737 and 1841 (*7*, *9*–*12*), the catastrophic 1952 earthquake (*13*–*17*), and several more recent events of moment magnitude (M_w) > 7.5 (Fig. 1A). These underthrusting earthquakes cause strong ground shaking, and the largest ones generate trans–Pacific tsunamis, making the Kuril-Kamchatka Trench a key focus of global seismic and tsunami hazard research. Geodetic observations indicate that the Kamchatka plate boundary was accumulating substantial strain along the 1952 rupture zone before the latest great earthquake (*18*).

On 29 July 2025, at 23:24:52 UTC, a great megathrust earthquake struck off the coast of the Kamchatka Peninsula, east-southeast of Petropavlovsk-Kamchatsky, Russia. This was the seventh largest seismologically recorded earthquake since 1900 (*19*). The hypocenter was 52.498°N, 160.264°E, at a depth of 35 km, as determined by the US Geological Survey National Earthquake Information Center (USGS-NEIC). The *W*-phase focal mechanism indicates thrust faulting, with the best double-couple strike of 198°, dip 18°, and rake 51°; a minor non–double-couple component (16%); and a seismic moment of 2.22×10^{22} N·m with a W-phase magnitude (M_{ww}) of 8.83 (Fig. 1A). Productive foreshock sequences near the hypocenter occurred in August 2024 and September 2025, with the largest event being a M_w 7.4 thrust event on 20 July 2025 at 06:49:04 UTC (fig. S1). The spatial distribution of early aftershocks (Fig. 1B) closely overlapped the aftershock region of the 1952 M_w 8.8 to 9.0 earthquake (*13*, *14*, *20*), and the 1952 hypocentral region also had intensive foreshock activity over several years before that event (*17*). This suggests that the 2025 event released accumulated strain along the same segment of the subduction interface. However, the 1952 event generated stronger tsunami waves in Hawaii (fig. S2) (*21*), indicating that the ruptures were not identical repeats.

To understand the rupture process of the 2025 M_w 8.8 Kamchatka earthquake, we first constrained the space-time slip distribution using teleseismic body and surface wave observations and InSAR (Interferometric Synthetic Aperture Radar) ground displacement measures, considering planar faulting and curved-plate interface faulting. We then performed forward tsunami calculations to validate our seismogeodetic slip models. The simulations for our preferred model with a curved plate boundary more successfully reproduced the observed tsunami timing and waveforms, as well as coseismic global navigation satellite system (GNSS)–sensed displacements, confirming the placement and strength of the associated rupture model. These results emphasize the value of joint seismic, geodetic, and tsunami analyses, especially for large offshore megathrust earthquakes with limited data sets.

Slip modeling and tsunami validation

To evaluate the influence of fault geometry on the inferred rupture behavior, we tested multiple configurations, including a simplified planar fault and a more realistic model with along-dip variations informed by the Slab2 geometry (*2*). We first constructed a rectangular fault plane that was based on the low-angle nodal plane of the *W*-phase moment tensor solution, with the strike slightly adjusted to 217° to align with the Kuril-Kamchatka Trench (model I) (fig. S3A). Using a nonlinear finite fault inversion algorithm [supplementary materials (SM), materials and methods], we constrained the spatiotemporal slip history using teleseismic waveforms (figs. S4 to S6). Model I indicated a complex rupture lasting ~300 s (fig. S3A), with a seismic moment of 2.25×10^{22} N·m (M_w 8.82). The inferred slip distribution was very heterogeneous, with a substantial shallow slip extending toward the trench (fig. S3A).

We then implemented a five-segment curved-fault model based on the Slab2 geometry (*2*), with dip angles varying from 6° in the shallowest segment to 33° in the deepest (model II) (fig. S3B), keeping all other modeling parameters unchanged and using the same data as for model I (figs. S7 and S8). This configuration introduced significant along-dip variations that substantially influenced the slip distribution. In contrast to model I, model II constrained the rupture to a narrow, elongated zone, with little shallow slip (fig. S3B), highlighting the strong influence of fault geometry on the resulting slip distribution. The rupture duration remained ~300 s (fig. S3B), and the total seismic moment was nearly identical at 2.26×10^{22} N·m (M_w 8.82).

Last, we refined the inversion by incorporating InSAR line-of-sight (LOS) displacements over southern Kamchatka (figs. S9 and S10), balancing the data weighting by expanding the seismic data (model III) (fig. S11). Model III has a ~280-s duration unilateral southwestward expansion of the rupture with an elongate ~250-km-long patch of slip exceeding 4 m, with a peak slip of ~14 m offshore of southern Kamchatka and along Paramushir Island (Fig. 2A). This is similar to model II but has substantial differences from both model I and the USGS-NEIC three-segment fault model (fig. S3). The rupture initiated at a depth of 22 km with relatively minor slip (<3 m) and initially propagated at ~1 km/s during the first 80 s (figs. S12 and S13). It then accelerated to ~2.5 km/s as it expanded southwestward. By 100 s, the rupture had reached shallow depths near the trench and continued propagating in the same direction. The main rupture ceased at around 180 s (fig. S13). Large interplate aftershocks from the Global Centroid Moment Tensor (GCMT) database exhibit a complementary distribution to the coseismic slip, filling in gaps or outlining edges of large-slip zones (Fig. 2A). Model III can well explain

[1]Hubei Subsurface Multi-Scale Imaging Key Laboratory, School of Geophysics and Geomatics, China University of Geosciences, Wuhan, China. [2]State Key Laboratory of Geological Processes and Mineral Resources, China University of Geosciences, Wuhan, China. [3]Marine Science and Technology College, Zhejiang Ocean University, Zhoushan, Zhejiang, China. [4]Donghai Laboratory, Zhoushan, Zhejiang, China. [5]Ocean College, Zhejiang University, Zhoushan, Zhejiang, China. [6]Department of Earth and Planetary Sciences, University of California, Santa Cruz, CA, USA. [7]School of Geodesy and Geomatics, Wuhan University, Wuhan, China. [8]Department of Geophysical Engineering, The Faculty of Mines, İstanbul Technical University (ITU), Ayazaga Campus, Maslak, Sarıyer, İstanbul, Türkiye. [9]Disaster Management Institute, ITU, Ayazaga Campus, Maslak, Sarıyer, İstanbul, Türkiye. ***Corresponding author. Email: liuchengli@cug.edu.cn (C.L.); yfbai@zju.edu.cn (Y.B.)**

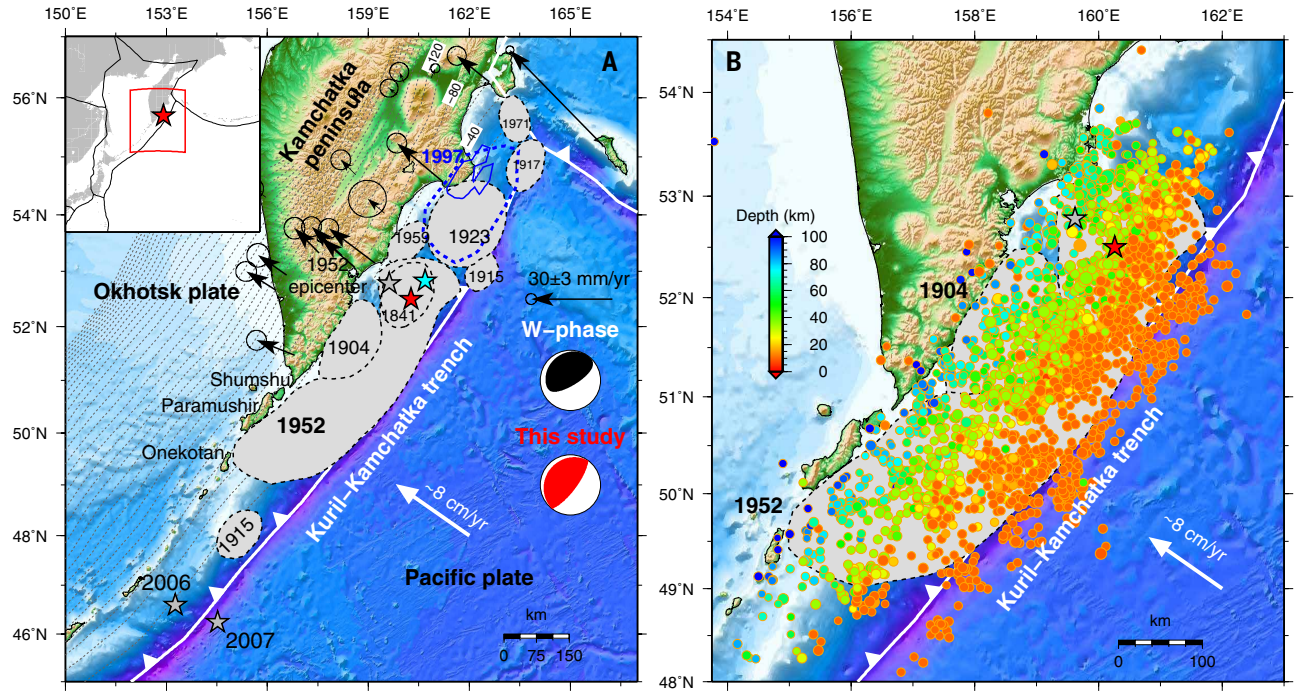

Fig. 1. Tectonic setting of the 29 July 2025 Kamchatka earthquake. (**A**) Gray-filled patches with dashed outlines indicate the aftershock regions of historical events. Blue dashed and solid contours indicate the aftershock region and rupture area of the 1997 event, respectively (*7*). The gray star indicates the epicenter of the 1952 earthquake, and the cyan and red stars indicate the epicenters of the 20 July 2025 M_w 7.4 foreshock and the 29 July 2025 M_w 8.8 mainshock, respectively. Trenches are indicated with white solid lines with barbs, and the white arrow indicates the relative motion between the Pacific Plate and the Okhotsk Plate. Black vectors indicate interseismic GPS velocities in the Kamchatka region (*18*). Depth contours to the subducting plate interface from the Slab2 model (*2*) are indicated with gray dashed lines at 20-km intervals. Focal mechanisms are shown in black for the *W*-phase solution and in red for those obtained in this study. (Inset) The general location of the study area. (**B**) Comparison between the aftershock distribution of the 2025 event during the first 3 months and the rupture zones of the 1904 and 1952 earthquakes.

both InSAR (fig. S10) and teleseismic observations (figs. S14 and S15) and also provides better fits than the other models for the currently published Kamchatka GNSS-sensed coseismic displacements (fig. S16). All models indicated relatively small slip (<5 m) near the hypocenter where the intense foreshock and larger aftershock activity occurred (Fig. 2 and figs. S1 and S12), and all have unilateral southwestward propagation overlapping the estimates of the large-slip area of the 1952 event inferred from tsunami data (*16*, *17*). The strong unilateral slip effects are clearly evident in long-period surface wave spectral analysis (*22*) for the event (fig. S17). The slip distribution is relatively simple compared with other events of this size that have well-studied ruptures (for example, the 1960 M_w 9.5 Chile, 1964 M_w 9.2 Alaska, 2004 M_w 9.2 Sumatra-Andaman, 2010 M_w 8.8 Chile, and 2011 M_w 9.1 Japan earthquakes).

To evaluate the reliability of the slip models, we conducted forward modeling of tsunami waveforms by calculating vertical seafloor and land surface deformation (fig. S18) and compared the results with observations from 22 Deep-ocean Assessment and Reporting of Tsunami (DART) stations (Fig. 3A). We tested our three slip models and the USGS-NEIC three-segment model (SM materials and methods). Model I and the USGS-NEIC three-segment model both failed to accurately reproduce the tsunami waveforms, particularly in terms of arrival times and waveform, with notable mismatches at DART stations located east of the epicenter (figs. S19 and S20). Moreover, the USGS-NEIC three-segment model, which features a maximum slip that exceeds 40 m, substantially overestimated the tsunami amplitudes (fig. S20). Model II showed great improvements, capturing both the timing and waveform characteristics more accurately (fig. S21). The best overall fit was achieved with model III, which provided good predictions of the observed tsunami amplitudes and waveforms (Fig. 3B), supported by the resolution and fault geometry tests (figs. S22 and S23), making it the preferred model for broadband motions of periods longer than about 5 s (shorter period motions are not resolved owing to the lack of available near-field recordings). The shallow slip distribution in model III is in good agreement with the US National Oceanic and Atmospheric Administration (NOAA) tsunami source, which also produced a good fit to the nearby DART data (*23*). These validation results emphasize the importance of incorporating accurate fault geometry, especially dip variations, and applying appropriate weighting across diverse data types to achieve robust rupture models in subduction zones with limited observational constraints.

Distinct foreshock sequences and rupture heterogeneity

Relative to the well-known foreshock sequences preceding the 2014 Iquique, Chile, earthquake (M_w 8.1) and 2011 Tohoku, Japan, earthquake (M_w 9.0) (*24*), a distinctive feature of the 2025 M_w 8.8 Kamchatka earthquake was the occurrence of two highly productive foreshock sequences over the prior year (fig. S1). The first foreshock sequence began on 17 August 2024 with a M_w 7.0 earthquake, and the second started on 20 July 2025 with an M_w 7.4 event. The migration directions of these two sequences were markedly different (fig. S1). The deeper 2024 foreshocks migrated upward and after 2 days reached the region where the 2025 foreshock sequence later occurred (fig. S1C), suggesting a stress-loading effect. The shallower 2025 foreshock sequence showed rapid migration southwestward up-dip of the mainshock hypocenter (fig. S1D), apparently triggering nucleation of the mainshock. Both sequences occurred far northeast of the main large-slip area and reflect a progressive failure-onset process. Their spatial distribution, on the periphery of the mainshock hypocenter, implies stress transfer and possible aseismic deformation along adjacent fault segments, potentially weakening the fault before rupture (*25*). However, no clear geodetic

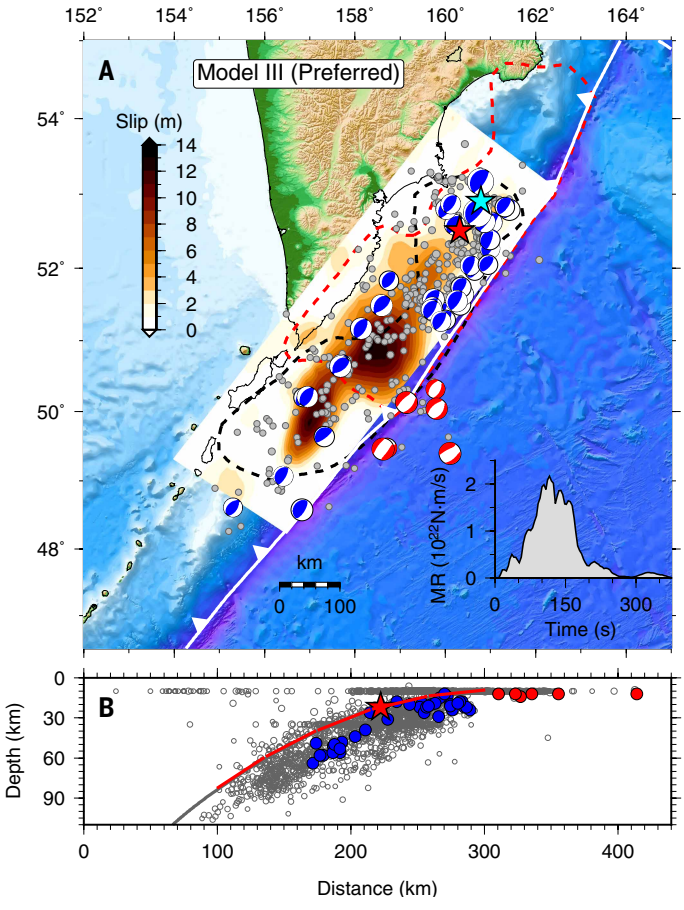

Fig. 2. Preferred slip model of the 29 July 2025 M_w 8.8 mainshock. (**A**) Slip model derived from joint inversion of teleseismic and InSAR data. The black and red dashed contours outline the aftershock zone of the 1952 earthquake and the interseismic coupling region (*18*), respectively. GCMT focal mechanisms are superimposed on the slip models, with normal faulting events indicated in red and thrust faulting indicated in blue, and the size is scaled by moment magnitude. The cyan and red stars indicate the epicenters of the 20 July 2025 M_w 7.4 foreshock and the 29 July 2025 M_w 8.8 mainshock, respectively. Gray circles indicate aftershocks ($M_w \geq 5.0$) within the first 3 months from the USGS-NEIC catalog. (Inset) The moment rate functions. (**B**) A cross section of the model geometry and the aftershock distribution from the USGS-NEIC catalog. The red and blue solid circles indicate the locations of the GCMT focal mechanisms illustrated in (A).

evidence of precursory slow slip was observed at the GNSS station in Petropavlovsk (PETT).

The inverted rupture pattern of the 2025 M_w 8.8 Kamchatka earthquake is notably characterized by a spatially confined large slip concentrated in the 15- to 30-km-depth range on the megathrust, with a little slip near the trench and closely corresponding to the identified zone of potential great earthquakes along the Kamchatka arc (*26*). Geodetic studies had identified a highly coupled megathrust zone overlapping much of the 1952 aftershock area (Fig. 2A) (*18*), which is consistent with decades of strain accumulation. However, the 2025 mainshock rupture was spatially limited to only about half of the inferred coupled zone and extended southwestward along Paramushir Island into an area of geodetically inferred lower coupling (Fig. 2A), although occurrence of a large, deep, outer-rise compressional event in 2020 suggested large compressional strain accumulation there (*27*). This suggests that along-strike variations in frictional properties, structural segmentation, or stress heterogeneity played a key role in constraining rupture propagation (*28*, *29*).

Coseismic slip near the hypocenter was modest (<5 m) and located slightly up-dip from the hypocenter. This indicates that the main rupture nucleated in a relatively weak, partially locked area (*18*), with a much greater slip concentrated about 100 km along-strike from the initiation point. The distribution of vigorous foreshock activity, encircling but not overlapping the zone of hypocentral slip, suggests that the nucleation process may have been influenced by complex local stress conditions and fault heterogeneity, and a similar process appears to have preceded the 1952 rupture that nucleated nearby.

The 2025 Kamchatka earthquake was the seventh instrumentally recorded megathrust event to have a magnitude of at least 8.8. Although similar in magnitude to the 27 February 2010 Maule earthquake in Chile, the two events exhibited striking differences in rupture behavior, slip pattern, and tsunami impact (fig. S24 and table S1). The 2025 Kamchatka earthquake exhibited a highly elongated, southwestward unilateral rupture with a single large-slip patch. It lacked sizable shallow slip extending to near the trench but did have outer-rise normal faulting seaward of the large-slip region (Fig. 2), apparently with a seaward-dipping pattern as indicated by a Coulomb stress change analysis (fig. S25). By contrast, the Maule earthquake featured a bilateral rupture with a heterogeneous slip distribution, prominent shallow slip in two patches along the megathrust, and intensive normal faulting in the outer-rise region seaward of the two shallow large-slip zones (*30*), as also observed for the 2011 Tohoku and 2006 Kuril events (*31*). Shallow large slip was associated with stronger tsunami generation for the 2006 Kuril, 2010 Maule, and 2011 Tohoku events. The peak slip during the Kamchatka earthquake (~14 m) was slightly lower than that of the Maule event (~17 m) (*32*), despite the Kamchatka event having a longer rupture duration than both the 2010 Maule and 2011 Tohoku events. This reflects differences in stress drop, rupture velocity, frictional properties, and coupling degree along the plate interfaces.

These differences emphasize that earthquake magnitude alone does not determine tsunami potential or rupture complexity (*33*). The depth and distribution of slip, rupture directivity, and coupling conditions at the plate interface play critical roles. The relatively uniform slip patch of the 2025 Kamchatka event indicates a tightly confined rupture lacking near trench slip, potentially because of structural barriers, presence of clay, or variations in pore fluid pressure along the plate boundary (*12*). This analysis underlines the need for region-specific hazard assessments and the importance of integrating geodetic, seismic, and tsunami data to understand rupture dynamics and associated hazards in subduction zones.

Earthquake supercycle

It is widely accepted that large megathrust earthquakes release a substantial portion of the strain accumulated during the interseismic period, resetting the slip and moment deficit (*34*). The 2025 Kamchatka earthquake largely overlapped the rupture area of the 1952 event and exhibited a peak slip of ~14 m versus peak slip of ~10 to 12 m for the 1952 rupture (Fig. 4A). Given an estimated convergence rate of ~8 cm/year (*3*), the expected slip deficit since 1952 would have been approximately 6 m. This implies that both the peak and average slip of the large-slip region in the 2025 event substantially exceeded the anticipated deficit. However, in the epicentral region, the slip closely matches the slip deficit since 1952, suggesting that the same nucleation patch may have ruptured in both events, effectively releasing most of the local deficit. An alternative possibility is that the epicentral region may not efficiently accumulate strain, owing to frequent release by multiple major earthquakes, including the 2024 M_w 7.0 and 2025 M_w 7.4 foreshocks, as well as the two large aftershocks on 13 September 2025 (M_w 7.4) and 18 September 2025 (M_w 7.8). This pattern highlights substantial strength heterogeneity along the subduction interface (fig. S14).

If the 1952 earthquake (M_w ~ 8.8 to 9.0) is considered to have released the slip deficit accumulated over roughly 215 years since the Kamchatka-spanning 1737 event (M_w ~ 9.3) (*7*), the estimated slip would have been

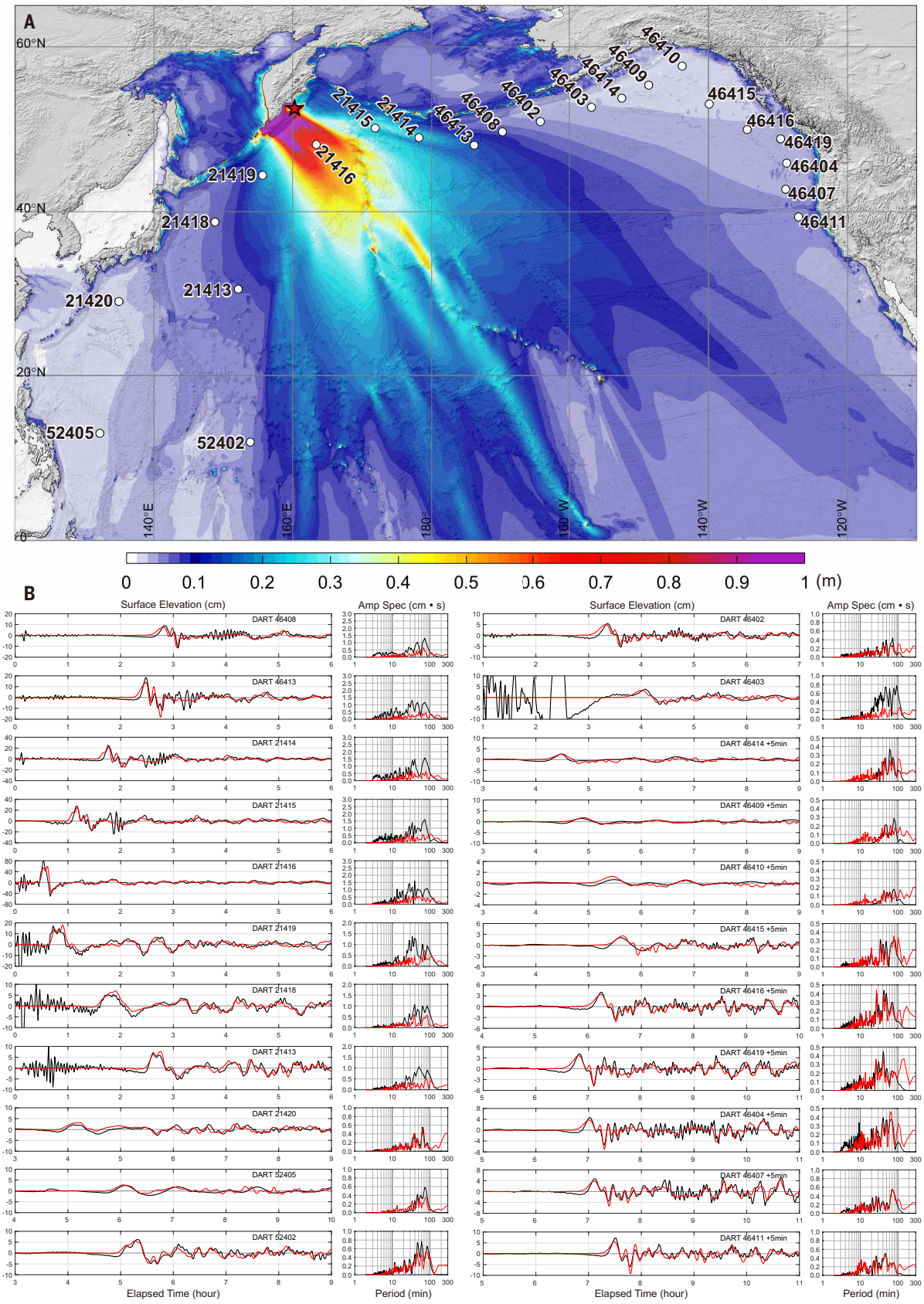

Fig. 3. Tsunami predictions for the preferred slip model in Fig. 2A. (**A**) Maximum sea surface elevation maps extending from the source region across the whole North Pacific predicted from the preferred model shown in Fig. 2A. DART stations are indicated with white dots, with station names labeled close by. The red star indicates the epicenter of the 2025 M_w 8.8 mainshock. (**B**) Comparison of observed and simulated tsunami waveforms for model III shown in Fig. 2A. Black lines indicate (left) observed time series and (right) amplitude spectra, and the predictions are indicated with red lines.

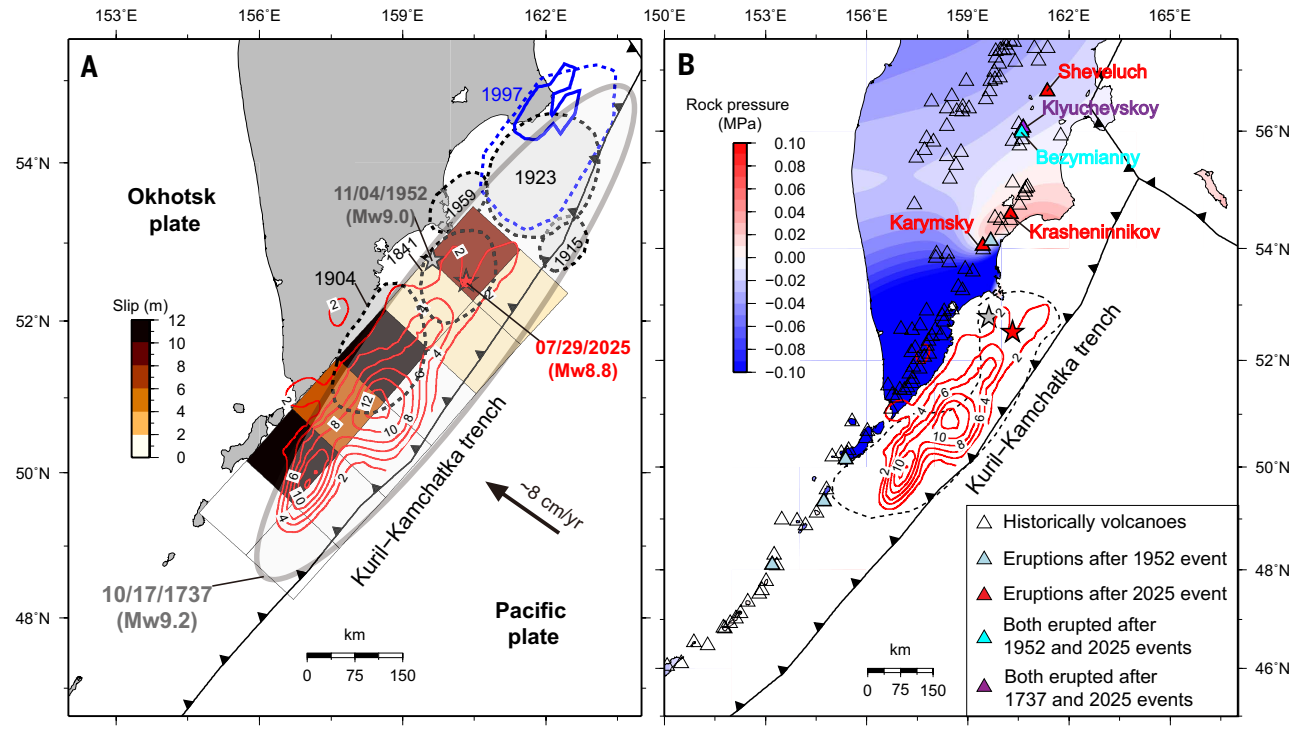

Fig. 4. Great earthquakes and their interaction with volcanoes along the southern Kamchatka subduction zone. (**A**) Comparison between the 2025 M_w 8.8 earthquake and previous large events. Red contours indicate the preferred slip model of the 2025 event. Colored rectangles indicate the slip distribution of the 1952 earthquake inferred from tsunami data (*16*). The gray ellipse indicates the estimated rupture area of the 1737 earthquake (*7*). Black dashed contours outline the historical rupture areas of the 1841, 1904, 1915, 1923, and 1959 events, respectively. Blue dashed and solid contours indicate the aftershock region and rupture area of the 1997 earthquake, respectively (*8*). (**B**) The 1952 and 2025 Kamchatka great earthquake rupture areas together with historical volcanoes. The white triangles indicate the historical volcanoes, and colored triangles indicate volcanoes that erupted in association with the 1737, 1952, and 2025 great earthquakes. The colored basemap depicts the rock pressure change field caused by the 2025 event.

about 17 m. Therefore, the 1952 event may not have released all accumulated strain. A large event in 1841 that produced a tsunami runup in central Kamchatka comparable with the 1737 and 1952 events (*11*) may have reduced strain in the northern portion of the 1952 and 2025 rupture zones (Fig. 4A), with other large events located farther northeast in 1923, 1959, and 1997 (*35*). The cumulative earthquake occurrence since 1737 indicates a segmented rerupture pattern. This behavior may be influenced by structural complexities such as the subduction of the Krusenstern fracture zone (*36*). The 2025 event may have released the remaining deficit in the southern portion of the 1737 rupture zone, suggesting a cascading release of strain that had built up over centuries. Geodetic observations indicate that north of 53°N, the subduction interface undergoes substantial aseismic slip, which corresponds to the lower seismic moment ($M_w \leq 8.5$) of earthquakes along this segment (*18*). By contrast, the southern portion of the rupture zone has experienced fewer clustered large events and longer periods of seismic quiescence.

This behavior reflects an earthquake supercycle (*37*–*40*), in which great megathrust earthquakes repeatedly rupture the same subduction zone segment at irregular intervals through complex patterns of strain accumulation, partial ruptures, aseismic slip, and episodic full ruptures. The sequence of earthquakes since 1737 along southern Kamchatka provides evidence for such a supercycle and further confirms numerical modeling results showing that earthquake supercycles in subduction zones are controlled by the width of the seismogenic zone (*1*). This framework helps explain the irregular timing, segmented nature, and local variability of large ruptures along the Kamchatka subduction zone, as well as differences in tsunami generation between successive events.

Recognition of supercycle characteristics has important implications for future seismic hazard assessments, particularly in subduction zones that have recently experienced great earthquakes. For example, the 2016 Chiloé M_w 7.6 earthquake in southern Chile may have signaled renewed seismic activity along the south-central Chile megathrust within the broad 1960 M_w 9.5 Valdivia earthquake rupture zone (*41*). Seismic hazard assessments based on an idealized earthquake cycle that assumes regular recurrence within fixed segments can underestimate the true risk. A more realistic framework that incorporates episodic, incomplete, and spatially heterogeneous strain release provides a better basis for evaluating potential seismic hazards in subduction zones worldwide.

Earthquake-volcano interactions

The Kamchatka Peninsula is one of the most volcanically active regions worldwide, with more than 300 volcanoes, many of which remain active (*42*). Large earthquakes can trigger volcanic unrest or eruptions through stress changes that perturb magmatic and hydrothermal systems, particularly in volcanoes already near a critical state (*43*–*46*). Historical records show that both the 1737 and 1952 great earthquakes in Kamchatka were followed by increased volcanic activity (*7*, *45*). The 1737 event triggered widespread eruptions, such as the eruption of the Klyuchevskoy volcano, which was the strongest eruption in the recent history of Kamchatka. After the 1952 earthquake, the volcano Bezymianny reawakened in 1955 and has remained persistently active ever since (*47*). After the 2025 earthquake, multiple eruptions were again observed (Fig. 4B and fig. S26). These include renewed activity at the volcanoes Klyuchevskoy and Bezymianny, which also erupted after the 1737 and 1952 events, respectively, highlighting their susceptibility to

seismic perturbations. In addition, 3 days after the mainshock, the volcano Krasheninnikov erupted for the first time since 1550 (fig. S26).

To quantitatively estimate the earthquake's potential impact on volcanic eruptions, we calculated the coseismic rock pressure change (*P*; as defined by eq. S1) experienced by the magma chambers after the earthquake (SM materials and methods). The results indicate that the 2025 M_w 8.8 Kamchatka earthquake likely affected several nearby volcanic eruptions, with the Krasheninnikov volcano experiencing relatively large coseismic compression (Fig. 4B and fig. S27), which likely contributed to promoting its centers. Although earthquakes can trigger eruptions through promoting gas exsolution and overpressure in magma chambers, mobilizing trapped bubbles, volumetric deformation, and increasing permeability in the surrounding rocks, particularly in volcanoes nearing eruption and located within a few fault lengths of the rupture zone (*43*–*46*, *48*–*50*), the specific triggering mechanism remains difficult to quantify. Volcanoes in Kamchatka (Fig. 4B) characterized by vertical, pipe-shaped conduits (such as Klyuchevskoy); shallow, dispersed magma and gas reservoir systems (such as Bezymianny); or low-viscosity, volatile-saturated basaltic magmas (such as Tolbachik) (*51*, *52*) appear more susceptible to seismic triggering, potentially advancing eruption timing. Overall, the critical state of a volcano varies greatly across systems and may manifest in different ways, making earthquake-induced eruptions highly dependent on the specific dynamics of each volcanic system. Detailed modeling of each volcanic system will be required to fully quantify the interactions between earthquake and volcano.

Nevertheless, the repeated observation of volcanic eruptions after great earthquakes in Kamchatka provides compelling evidence of earthquake-volcano interactions. These findings highlight the importance of closely monitoring volcanoes situated in great earthquake rupture zones (for example, the 1960 Chile M_w 9.5, 1964 Alaska M_w 9.2, and 2004 Sumatra-Andaman M_w 9.2 earthquakes) and incorporating earthquake-induced volcanic hazards into future eruption forecasting and hazard mitigation strategies. This is particularly relevant for governmental agencies responsible for issuing volcanic alerts.

REFERENCES AND NOTES

1. R. Herrendörfer, Y. Van Dinther, T. Gerya, L. A. Dalguer, *Nat. Geosci.* **8**, 471–474 (2015).
2. G. P. Hayes *et al.*, *Science* **362**, 58–61 https://www.science.org/doi/10.1126/science.aat4723 (2018).
3. C. DeMets, R. G. Gordon, D. F. Argus, *Geophys. J. Int.* **181**, 1–80 (2010).
4. J. Kelleher, L. Sykes, J. Oliver, *J. Geophys. Res.* **78**, 2547–2585 (1973).
5. V. M. Zobin, *Bull. Seismol. Soc. Am.* **86**, 811–820 (1996).
6. O. J. Pérez, *Bull. Seismol. Soc. Am.* **90**, 1096–1100 (2000).
7. V. K. Gusiakov, "Two Great Kamchatka Tsunamis, 1737 and 1952. IUGG Tsunami Commission" (Institute of Computational Mathematics and Mathematical Geophysics, Siberian Division, Russian Academy of Sciences, 2000); https://bibliotecadigital.ciren.cl/handle/20.500.13082/28986.
8. V. M. Zobin, V. I. Levina, *Bull. Seismol. Soc. Am.* **91**, 1619–1628 (2001).
9. S. A. Fedotov *et al.*, *Tectonophysics* **9**, 249–258 (1970).
10. T. Rikitake, *Tectonophysics* **35**, 335–362 (1976).
11. T. K. Pinegina *et al.*, *Pure Appl. Geophys.* **175**, 1485–1506 (2018).
12. T. K. Pinegina *et al.*, *Quat. Sci. Rev.* **233**, 106171 (2020).
13. M. Båth, H.Benioff, *Bull. Seismol. Soc. Am.* **48**, 1–15 (1958).
14. A. Ben-Menahem, M. N. Toksöz, *J. Geophys. Res.* **68**, 5207–5222 (1963).
15. H. Kanamori, *Phys. Earth Planet. Inter.* **11**, 216–226 (1976).
16. J. M. Johnson, K. Satake, *Pure Appl. Geophys.* **154**, 541–553 (1999).
17. B. T. MacInnes, R. Weiss, J. Bourgeois, T. K. Pinegina, *Bull. Seismol. Soc. Am.* **100**, 1695–1709 (2010).
18. R. Bürgmann *et al.*, *J. Geophys. Res.* **110**, 2005JB003648 (2005).
19. H. Benz *et al.*, The 29 July 2025, *M* 8.8 Kamchatka Earthquake, U.S. Geological Survey StoryMap (USGS, 2025); https://earthquake.usgs.gov/storymap/index-kamchatka2025.html.
20. E. A. Okal, *Pure Appl. Geophys.* **139**, 17–57 (1992).
21. National Geophysical Data Center/World Data Service, NCEI/WDS Global Historical Tsunami Database, NOAA National Centers for Environmental Information; https://doi.org/10.7289/V5PN93H7.
22. H. Kanamori, J. W. Given, *Phys. Earth Planet. Inter.* **27**, 8–31 (1981).
23. NOAA PMEL Center for Tsunami Research, Kamchatka Tsunami, July 29, 2025 Main Event 436 Page, NOAA NCTR research product (NOAA, 2025); https://nctr.pmel.noaa.gov/kamchatka20250729.
24. E. E. Brodsky, T. Lay, *Science* **344**, 700–702 (2014).
25. M. Bouchon, V. Durand, D. Marsan, H. Karabulut, J. Schmittbuhl, *Nat. Geosci.* **6**, 299–302 (2013).
26. A. N. Besedina *et al.*, *Izv. Russ. Acad. Sci., Phys. Solid Earth* **61**, 175–188 (2025).
27. L. Ye, T. Lay, H. Kanamori, *Earth Planet. Sci. Lett.* **556**, 116728 (2021).
28. C. H. Scholz, *Nature* **391**, 37–42 (1998).
29. T. Lay *et al.*, *J. Geophys. Res. Solid Earth* **117**, B04311 (2012).
30. A. Sladen, J. Trevisan, *Earth Planet. Sci. Lett.* **483**, 105–113 (2018).
31. T. Lay, L. Ye, Z. Wu, H. Kanamori, *J. Geophys. Res. Solid Earth* **125**, e2020JB020137 (2020).
32. H. Yue *et al.*, *J. Geophys. Res. Solid Earth* **119**, 7786–7804 (2014).
33. K. F. Cheung, T. Lay, L. Sun, Y. Yamazaki, *Nat. Geosci.* **15**, 33–36 (2022).
34. H. Kanamori, E. E. Brodsky, *Phys. Today* **54**, 34–40 (2001).
35. A. A. Gusev, L. S. Shumilina, *Izvest. Phys. Solid Earth* **40**, 206–215 (2004).
36. C. Gaedicke *et al.*, in *AGU Fall Meeting Abstracts* (AGU, 2010), vol. 2010, pp. T11D–2123.
37. C. Goldfinger, Y. Ikeda, R. S. Yeats, J. Ren, *Seismol. Res. Lett.* **84**, 24–32 (2013).
38. B. Philibosian *et al.*, *J. Geophys. Res. Solid Earth* **119**, 7258–7287 (2014).
39. J. M. Nocquet *et al.*, *Nat. Geosci.* **10**, 145–149 (2017).
40. E. A. Wirth, V. J. Sahakian, L. M. Wallace, D. Melnick, *Nat. Rev. Earth Environ.* **3**, 125–140 (2022).
41. S. Ruiz *et al.*, *Geophys. Res. Lett.* **44**, 6633–6640 (2017).
42. A. Y. Ozerov, O. A. Girina, N. A. Zharinov, A. B. Belousov, Y. V. Demyanchuk, *J. Volcanol. Seismol.* **14**, 1–17 (2020).
43. D. P. Hill, F. Pollitz, C. Newhall, *Phys. Today* **55**, 41–47 (2002).
44. M. Manga, E. E. Brodsky, *Annu. Rev. Earth Planet. Sci.* **34**, 263–291 (2006).
45. T. R. Walter, F. Amelung, *Geology* **35**, 539–542 (2007).
46. G. Seropian, B. M. Kennedy, T. R. Walter, M. Ichihara, A. D. Jolly, *Nat. Commun.* **12**, 1004 (2021).
47. O. A. Girina *et al.*, *J. Volcanol. Seismol.* **14**, 394–409 (2020).
48. S. Eggert, T. R. Walter, *Tectonophysics* **471**, 14–26 (2009).
49. T. Nishimura, *Geophys. Res. Lett.* **44**, 7750–7756 (2017).
50. L. Caricchi, M. Townsend, E. Rivalta, A. Namiki, *Nat. Rev. Earth Environ.* **2**, 458–476 (2021).
51. I. Koulakov *et al.*, *J. Geophys. Res. Solid Earth* **122**, 3852–3874 (2017).
52. I. Koulakov *et al.*, *Sci. Rep.* **11**, 1758 (2021).

ACKNOWLEDGMENTS

We thank the two anonymous reviewers for their constructive comments. We thank R. Wang for his helpful discussions on earthquake-volcano interactions. We thank the Institute of Earthquake Prediction Theory and Mathematical Geophysics, Russian Academy of Sciences, for releasing the coseismic GNSS displacement map, which provided an opportunity to validate our slip models. We thank A. A. Emanov, D. Chebrov, and E. Matveenko of the regional catalog of Kamchatka Branch, Federal Research Center, Geophysical Survey, Russian Academy of Sciences (KB GS RAS) for sharing the seismicity catalogs. **Funding:** This work was supported by the National Natural Science Foundation of China, 42222403 (C.L.); National Key R&D Program of China, 2022YFF0800703 (C.L. and X.X.); National Natural Science Foundation of China, 42376212 (Y.B.); US National Science Foundation, EAR1802364 (T.L.); MOST Special Fund from State Key Laboratory of Geological Processes and Mineral Resources, China University of Geosciences, MSFGPMR2024-502 (C.L. and X.X.); and the Istanbul Technical University Research Fund, İTÜ-BAP (T.T.). **Author contributions:** Conceptualization: C.L., Y.B., T.L. Methodology: C.L., Y.B. Investigation: C.L., Y.B., T.L., T. T. Visualization: C.L., Y.B. Funding acquisition: C.L., Y.B., T.L., X.X. Project administration: C.L., Y.B., T.L., X.X. Supervision: C.L., Y.B., T.L., X.X. Writing – original draft: C.L., Y.B., T.L., P.H., Y.W., T.T. Writing – review & editing: T.L., P.H., Y.W., and T.T. **Competing interests:** Authors declare that they have no competing interests. **Data, code, and materials availability:** All data are available in the main text or the supplementary materials. The final slip model is available at https://doi.org/10.5281/zenodo.18466362 (*87*). The finite fault inversion code is publicly available on github repositories of USGS: https://code.usgs.gov/ghsc/neic/algorithms/neic-finitefault. All teleseismic data can be downloaded through the IRIS Wilber 3 system (https://ds.iris.edu/wilber3) and ORFEUS (https://www.orfeus-eu.org). The USGS-NEIC catalog are available from https://earthquake.usgs.gov/earthquakes/search; the regional catalog of Kamchatka Branch, Federal Research Center, Geophysical Survey, Russian Academy of Sciences is available from https://sdis.emsd.ru/info/earthquakes/catalogue.php. The moment tensor solutions come from the Global Centroid Moment Tensor project (CMT; http://www.globalcmt.org). The DART data can be obtained from NOAA (https://www.ndbc.noaa.gov/obs.shtml). The volcano information is available from the Activity of Volcanoes Kamchatka (https://www.emsd.ru/~ssl/monitoring/main.htm) and the Global Volcanism Program (https://volcano.si.edu). The historical tsunami height data are available from https://www.ngdc.noaa.gov/hazel/view/hazards/tsunami/related-runups/6044. The GNSS data and time series plots at station PETT are available from the Nevada Geodetic Laboratory (NGL; https://geodesy.unr.edu). No new physical materials were generated for this study.

SUPPLEMENTARY MATERIALS

science.org/doi/10.1126/science.aeb8232
Materials and Methods; Figs. S1 to S27; References (*53*–*87*)

Submitted 28 August 2025; accepted 9 January 2026

10.1126/science.aeb8232

Simple unilateral rupture of the great M_W 8.8 2025 Kamchatka earthquake

Chengli Liu, Yefei Bai, Thorne Lay, Ping He, Yangmao Wen, Xiong Xiong, and Tuncay Taymaz

Science **391** (6787), . DOI: 10.1126/science.aeb8232

Editor's summary

In late July 2025, a moment magnitude 8.8 earthquake struck off the Kamchatka Peninsula coast in Russia, sparking a trans-Pacific tsunami and triggering volcanic activity in the region. The event highlighted how the recurrence of great earthquakes may not follow regular patterns. Liu *et al.* combined teleseismic and satellite data with deep-water tsunami recordings to estimate the slip history for the 2025 event. Peak slip was greater than for the similarly located 1952 earthquake despite generating a weaker tsunami. Variable recurrence and slip distributions in this region suggest complex strain release patterns that may heighten seismic risk. —Angela Hessler

Science
AAAS

Supplementary Materials for

Simple unilateral rupture of the great M_w 8.8 2025 Kamchatka earthquake

Chengli Liu *et al*.

Corresponding authors: Chengli Liu, liuchengli@cug.edu.cn; Yefei Bai, yfbai@zju.edu.cn

Science **391**, 812 (2026)
DOI: 10.1126/science.aeb8232

The PDF file includes:

Materials and Methods

Teleseismic data

We selected teleseismic *P*-waves, *SH*-waves, and surface waveforms from the Incorporated Research Institutions for Seismology (IRIS) data management center, ensuring good azimuthal coverage and high signal-to-noise ratio within distances of 30° to 90° (figs. S4 and S11). For the inversion, we applied bandpass filters of 2-330 s to body waves and 166-333 s to surface waves. Initial alignment of body waves was based on theoretical *P*- and *SH*-wave arrival times calculated using the reviewed hypocenter location of the USGS-NEIC and travel-time tables of IASP91 (*53*), with subsequent minor adjustments manually guided by preliminary inversion results (*54*).

Geodetic data

We analyzed the coseismic surface deformation associated with the 29 July 2025 Kamchatka earthquake using Synthetic Aperture Radar (SAR) data acquired by the Sentinel-1A/C satellites in both ascending and descending orbits. The descending dataset corresponds to track T060D, spanning acquisitions from 19 July 2025 to 31 July 2025, while the ascending dataset corresponds to track T111A, spanning 23 July 2025 to 4 August 2025. Interferometric processing was performed using the GAMMA software package (*55*), following standard procedures including precise orbit correction, image co-registration, interferogram generation, adaptive filtering, and phase unwrapping. Topographic contributions were removed using the 30 m Shuttle Radar Topography Mission (SRTM) DEM (*56*), while atmospheric artifacts were corrected using the Generic Atmospheric Correction Online Service for InSAR (GACOS) (*57*).

The resulting interferograms exhibit high coherence across the onshore Kamchatka region (fig. S9), allowing for reliable retrieval of coseismic deformation. Line-of-sight (LOS) displacements range from -5 to 100 cm for descending track T060D and from -126 to 2 cm for ascending track T111A. Maximum LOS deformation approaches 1 m near the southeastern peninsula coast. The spatial pattern reveals significant subsidence in the hanging wall and uplift in the forearc, consistent with shallow reverse slip on the subduction interface. These results provide robust geodetic evidence for large thrust motion along the Kuril-Kamchatka subduction zone. For the final inversion, the interferograms were down sampled to a total of 2,219 points (figs. S10A and S10D).

To further verify the reliability of our models, using Didger 3 software (https://didger.software.informer.com/3.0/), we digitized the data from the GNSS coseismic displacement map released by Institute of Earthquake Prediction Theory and Mathematical Geophysics, Russian Academy of Sciences (https://www.itpz-ran.ru/en/rupture-model-of-the-kamchatka-megathrust-earthquake-of-29-july-2025-mw-8-7-8-8-derived-from-gnss-observations/), to tentatively compare with the displacements predicted from our slip models. We do not invert these data, as the final solutions and their uncertainties have not yet been fully released. Our preferred model fits the GNSS data very well, and we expect that if and when the precise data and uncertainties are released, their inclusion in joint inversions will not modify our preferred model significantly.

Finite fault inversion

We use a kinematic finite-fault inversion approach (*58*, *59*), which performs a space-time slip inversion in the wavelet domain for teleseismic body and surface waveforms (figs. S4 and S11), along with down-sampled InSAR-based ground deformation (figs. S10A and S10D). A simulated

annealing algorithm is employed to simultaneously invert for rake angle, rise time, slip amplitude, and average rupture velocity. For Model I, the fault plane is parameterized with 27 and 15 subfaults along the strike and dip directions, respectively. For Model II, the fault geometry adopts the dip direction and angle from the Slab2 model (*2*) and is discretized into 27 subfaults along strike and 18 along dip. Model III shares the same geometry as Model II but excludes the bottom three subfaults in the dip direction. All models use a uniform subfault size of 25 km (along strike) by 15 km (along dip). The hypocenter for Model I is set at 52.512°N, 160.324°E, with a depth of 35 km, based on the USGS-NEIC catalog. For Models II and III, the hypocenter is set at the same epicentral location but adjusted to 22 km depth to align with the Slab2 interface (*2*). Absolute depth of the interface is not tightly constrained in Slab2, so there is at least 5-10 km uncertainty in the absolute depths of slip in all models. During the inversions, slip is allowed to vary between 0.0 and 20.0 m, rise time is constrained between 3 and 30 s, rake angle between 6° and 156°, and rupture velocity between 0.5 and 3.5 km/s. To approximate the Earth's structure in the source region, we adopted a 1D layered velocity model interpolated from the global Crust1.0 dataset (*60*). Synthetic seismograms for body waves and long-period surface waves were computed using the first-motion approximation method (*61*) and the normal mode summation technique (*62*), respectively.

Joint inversions always present challenges in assigning relative weights to different datasets, especially for the highly uneven distribution of near-field datasets. In this study, considering the characteristics of the teleseismic waveforms and InSAR displacements, we adopted a trial-and-error approach to test various weight assignments for different datasets, guided by independent tsunami simulations (*63*, *64*). Ultimately, we allocated a weight of 1/8 to the InSAR data relative to the teleseismic waveforms.

Resolution test and model uncertainty analysis

Checkerboard tests provide a direct way to visualize the resolution of finite-fault inversions (*65*). Here, we conducted such analysis to assess the resolution of our joint inversion. Following the same procedure as for the real data, we used the identical fault geometry and subfault discretization as in Model III. The checkerboard pattern consisted of slip patches spanning 3×6 subfaults, with a size of 75 km × 90 km. Synthetic data were computed for the same stations as those used in the real-data inversions (figs. S10 and S11), employing the same Green's functions.

The results show that the joint inversion can successfully recover the rupture process and achieve high resolution across the entire fault model, particularly for slip near the trench (fig. S22). demonstrating that our joint inversion approach can provide a high-resolution and reliable rupture model for the 2025 M_W 8.8 Kamchatka earthquake.

Simulated annealing inversions often show slight sensitivity to the choice of random seed, as different seeds produce distinct initial fault models. To evaluate the impact of random seed selection and to characterize uncertainties of the Model III, we performed 50 finite-fault inversions for the mainshock, each initialized with a different random seed. All 50 inversions yielded similar results, the mean coseismic slip distribution and the associated standard deviation are shown in fig. S22. Slip variability is generally low across most of the fault, except for a patch in the southwestern portion of the fault.

We further assessed the influence of fault geometry by constructing three additional candidate models based on the Slab2 interface *(2)* and the aftershock distribution. All other parameters and inversion procedures were kept identical to those of Model III. These models were subsequently evaluated using tsunami simulations. Variations in dip angle have a pronounced effect on the

resulting slip distribution. Similar to the differences observed between Model I and Model II, the three test models can well the seismic waveforms and InSAR data but exhibit substantial differences in their tsunami predictions. All three models provide noticeably poorer fits to the tsunami observations than Model III (fig. S23). Therefore, Model III is considered the most robust and is adopted as our final preferred model.

Tsunami modeling

Tsunami recordings at far-field DART stations are modeled by the Non-hydrostatic Evolution of Ocean WAVE model (*66*) to validate the distribution of large slip during the 2025 Kamchatka earthquake. NEOWAVE is a well-established non-hydrostatic tsunami model that augments the nonlinear shallow-water equations with depth-averaged vertical velocity and nonhydrostatic pressure, enabling the modeling of quasi three-dimensional free-surface flow (*67*, *68*). The governing equations allow the model to accurately describe key tsunami processes, including generation from time-dependent seafloor deformation within finite rise time (*69*), frequency dispersion during trans-oceanic propagation (*70*, *71*), wavenumber-dependent shoaling on slopes (*72*), and sea-surface oscillations of runup and drawdown over steep topography (*73*, *74*). The numerical formulation is discretized upon a staggered finite difference scheme with two-way nested grids in spherical coordinates to describe multi-scale wave processes (*75*). Its performance has been comprehensively verified through theoretical analysis, numerical investigation, and benchmarking against mathematical models, numerical solutions, laboratory data, and field measurements (*76*). The model has been widely utilized to investigate earthquake and tsunami sources, near-field and far-field wave dynamics, and coastal inundation processes in historical and hypothetical events (*33*, *77-81*).

Given the inverted finite fault solution of each earthquake source model, the near-field evolution of seafloor displacement is obtained through the elastic half-space solution (*82*) to generate tsunamis for propagation (fig. S18). The vertical displacement at each time step is augmented by horizontal motion of the continental slope (*83*). The computational domain in this study extends across the northwest Pacific with a 2-arcmin (~3600 m) resolution to cover the earthquake source region and 22 DART stations for tsunami validation (Fig. 3A). The digital elevation model is obtained from GEBCO 2024 and Manning coefficients of 0.025 and 0.035 are utilized respectively to describe the roughness of the seafloor and terrain. The computation spans up to 16 hours of elapsed time to yield tsunami signals for comparison with the measurements in terms of time series and amplitude spectrum (figs. 3A, S19, S20, and S21).

Coulomb failure stress and rock pressure

The Coulomb failure stress (ΔCFS) change can be defined as (*84*): $\Delta CFS=\Delta\tau+\mu'\Delta\sigma_N$, where $\Delta\tau$ and $\Delta\sigma_N$ are changes in the shear stress and normal stress on a receiver fault, respectively, caused by the earthquake. In this study, the friction coefficient (μ') was set to 0.4, as a common choice. The values of $\Delta\tau$ and $\Delta\sigma N$ are defined with respect to the slip and normal directions of the receiver fault, respectively. Hence, the positive value of ΔCFS indicates that the earthquake-induced stress changes push the receiver fault closer to rupture, while a negative value of ΔCFS suggests the opposite.

Using the code PSGRN/PSCMP (*85*), we calculated the coseismic Coulomb stress change at outer-rise environments caused by the M_W 8.8 earthquake, for the receiver faults, we used two different dipping directions, averaged from the GCMT solutions shown in Figure 2. One nodal

plane dips east with strike=33°, dip=43° and rake=-100°, and the second nodal plane dips west with a strike=228°, dip=50° and rake=-80°.

In addition, to quantitatively estimate the earthguake's possible impact on the volcano eruptions, we also calculated the change of rock pressure (P) caused by the M_W 8.8 earthquake,

$$P=-(\sigma_1+\sigma_2+\sigma_3)/3, \quad \text{(S1)}$$

where $\sigma_{1,2,3}$ are the increases in the three principal stresses (positive in tension and negative in compression) after the earthquake.

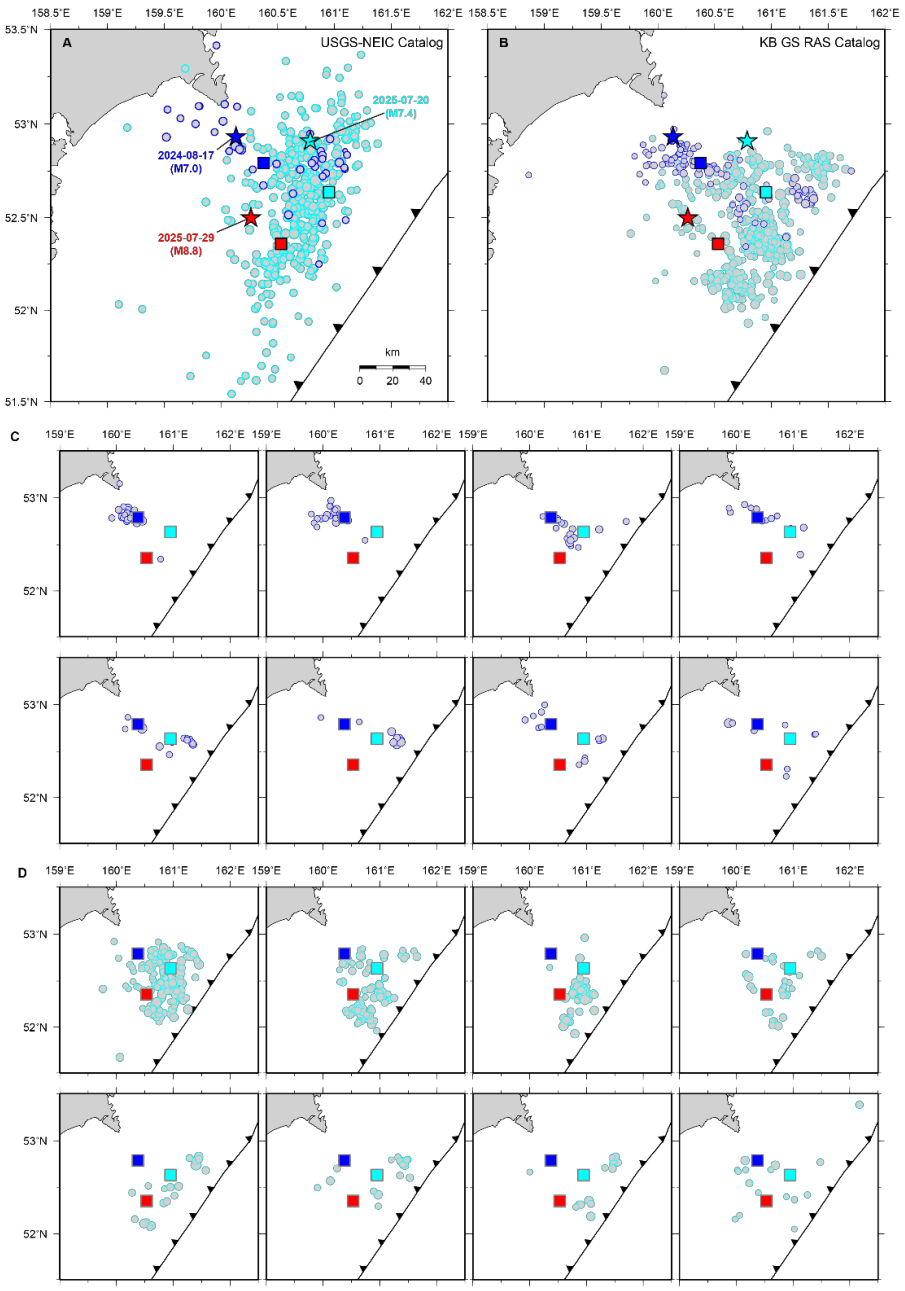

Fig. S1. Foreshock sequences and migrations before the mainshock. (A) and (B) show data from the USGS-NEIC and KB GS RAS catalogs, respectively. Stars indicate earthquake locations from the USGS-NEIC catalog, while squares represent those from the regional catalog of Kamchatka Branch, Federal Research Center, Geophysical Survey, Russian Academy of Sciences (KB GS RAS) catalog. There is a systematic discrepancy between the two catalogs; however, the KB GS RAS catalog contains a larger number of earthquakes. So, we use the KB GS RAS catalog to investigate the seismic migration 9 days after the 2024 M_W 7.0 earthquake (C) and the 2025 M_W 7.4 earthquake (D), respectively.

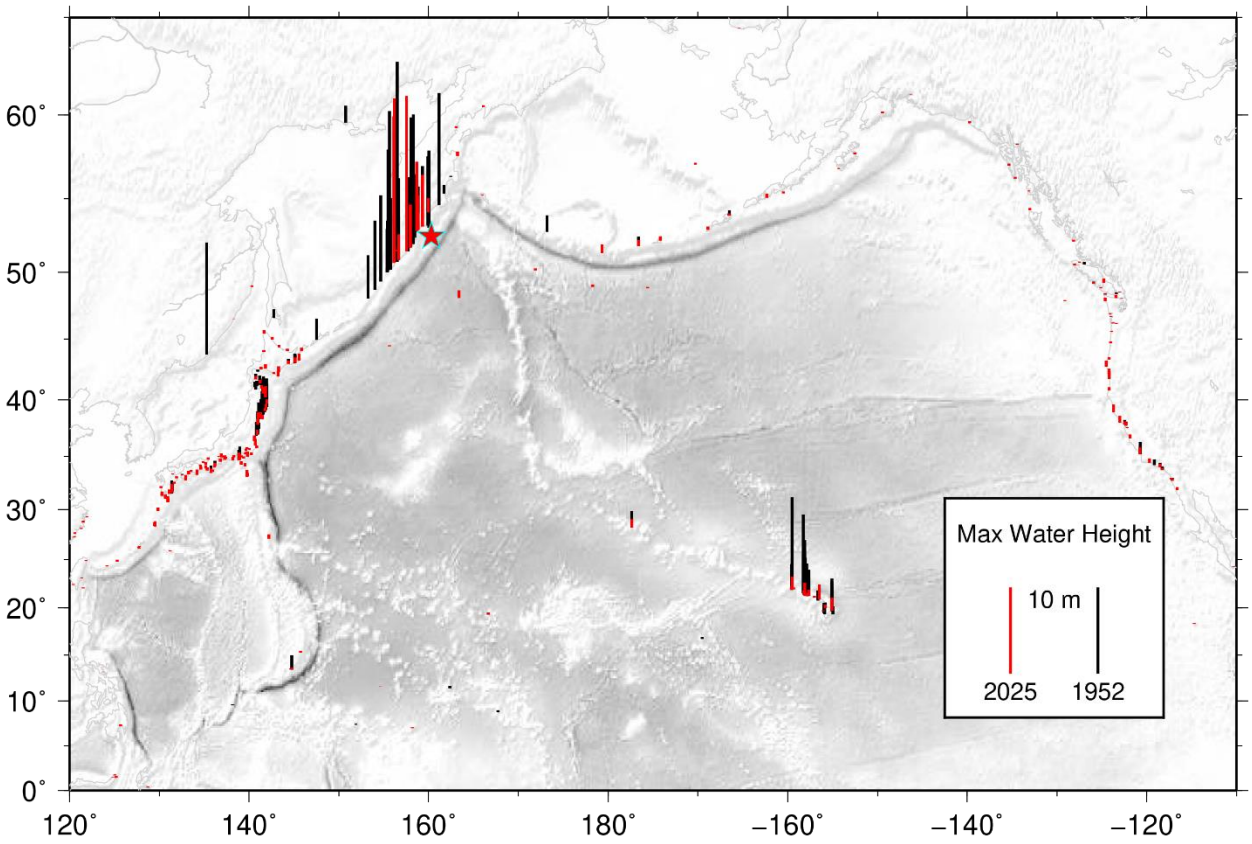

Fig. S2. Comparison of maximum tsunami wave heights generated by the 1952 and 2025 Kamchatka earthquakes (*21*). Note the significantly larger tsunami in 1952 observed in Hawaii. Observations for the Northern Kuril Islands are not yet available for 2025.

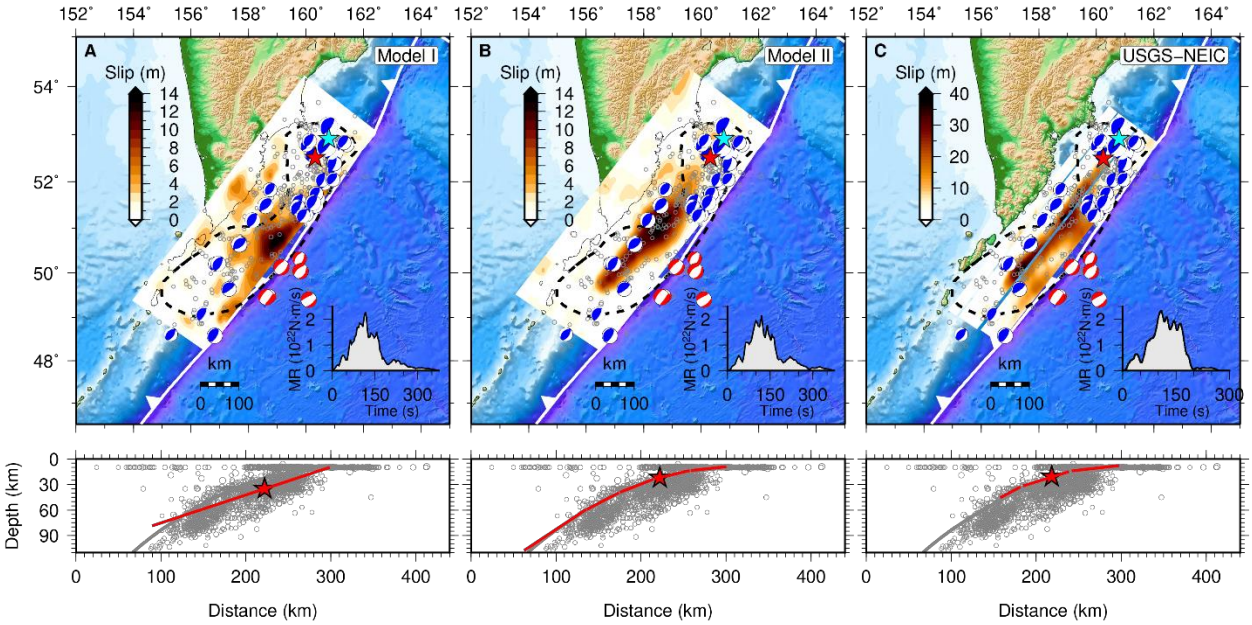

Fig. S3. Comparison of Slip Models. (A) and (B) Teleseismic slip models determined using a planar fault and a curved fault, respectively. (C) The final USGS-NEIC model, which includes 3 fault segments. The black dashed contour outlines the aftershock zone of the 1952 earthquake. GCMT focal mechanisms are superimposed on the slip models, with normal faulting events shown in red and others in blue, and the size is scaled by moment magnitude. The cyan and red stars indicate the epicenters of the 20 July 2025 M_W 7.4 foreshock and the 29 July 2025 M_W 8.8 mainshock, respectively. Gray circles show aftershocks ($M \geq 5.0$) within the first three months from the USGS-NEIC catalog. Insets in the bottom right corners of the upper panels show the moment rate functions. The lower panels display cross-sections of the three model geometries and the aftershock distribution from the USGS-NEIC catalog.

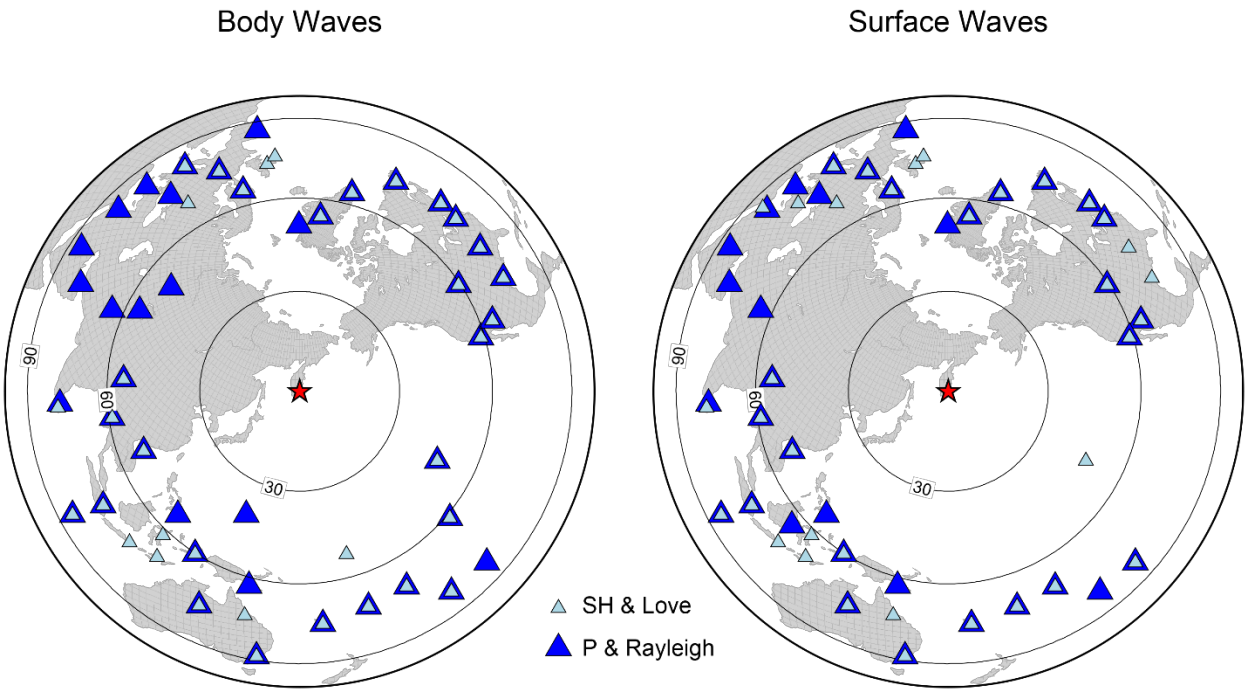

Fig. S4. Distributions of teleseismic broadband stations providing body-wave (left) and surface-wave (right) ground displacement observations used in the inversions for Model I and Model II.

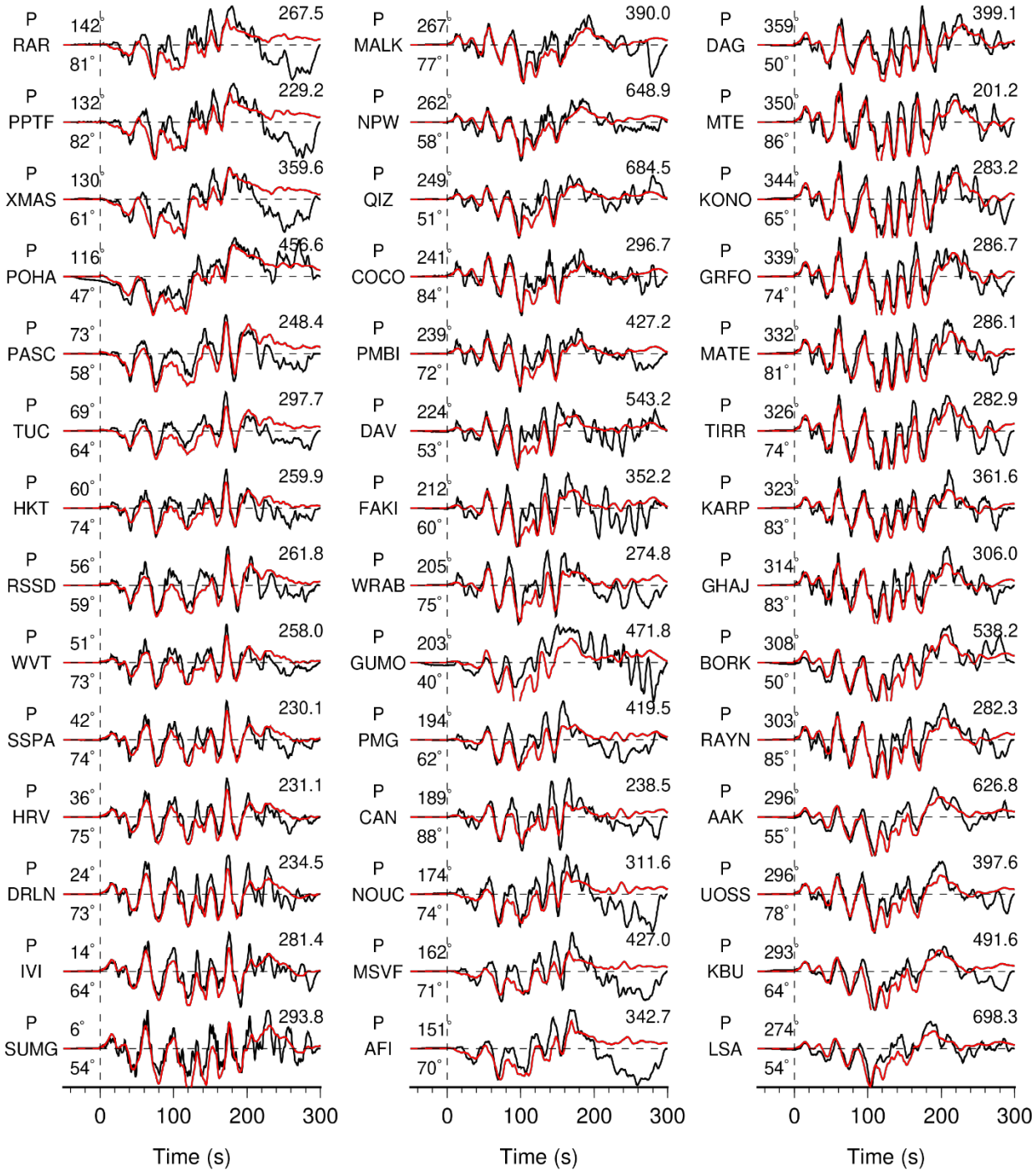

Fig. S5. Comparison of observed (black) and synthetic (red) teleseismic *P* wave ground displacements for Model I shown in fig. S3A. Data and synthetic seismograms are manually aligned on the first arrivals. Station names and phase-type are indicated on the left of each comparison. The azimuth (above) and epicentral distance (below) in degrees are shown at the beginning of each record. The number above the right portion of each comparison is the peak amplitude of the observed ground displacement in μm.

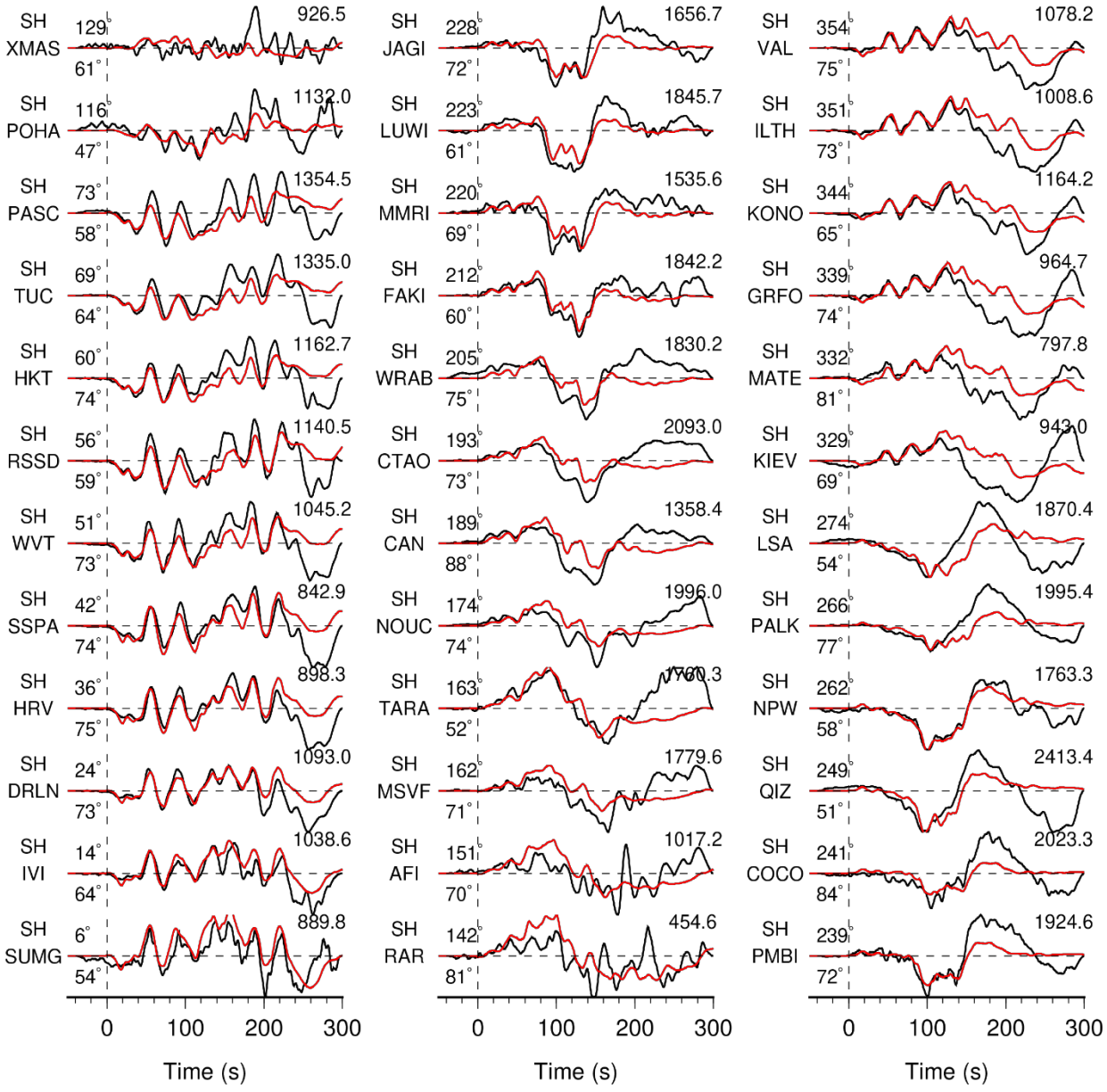

Fig. S5. Continued, for *SH* waves.

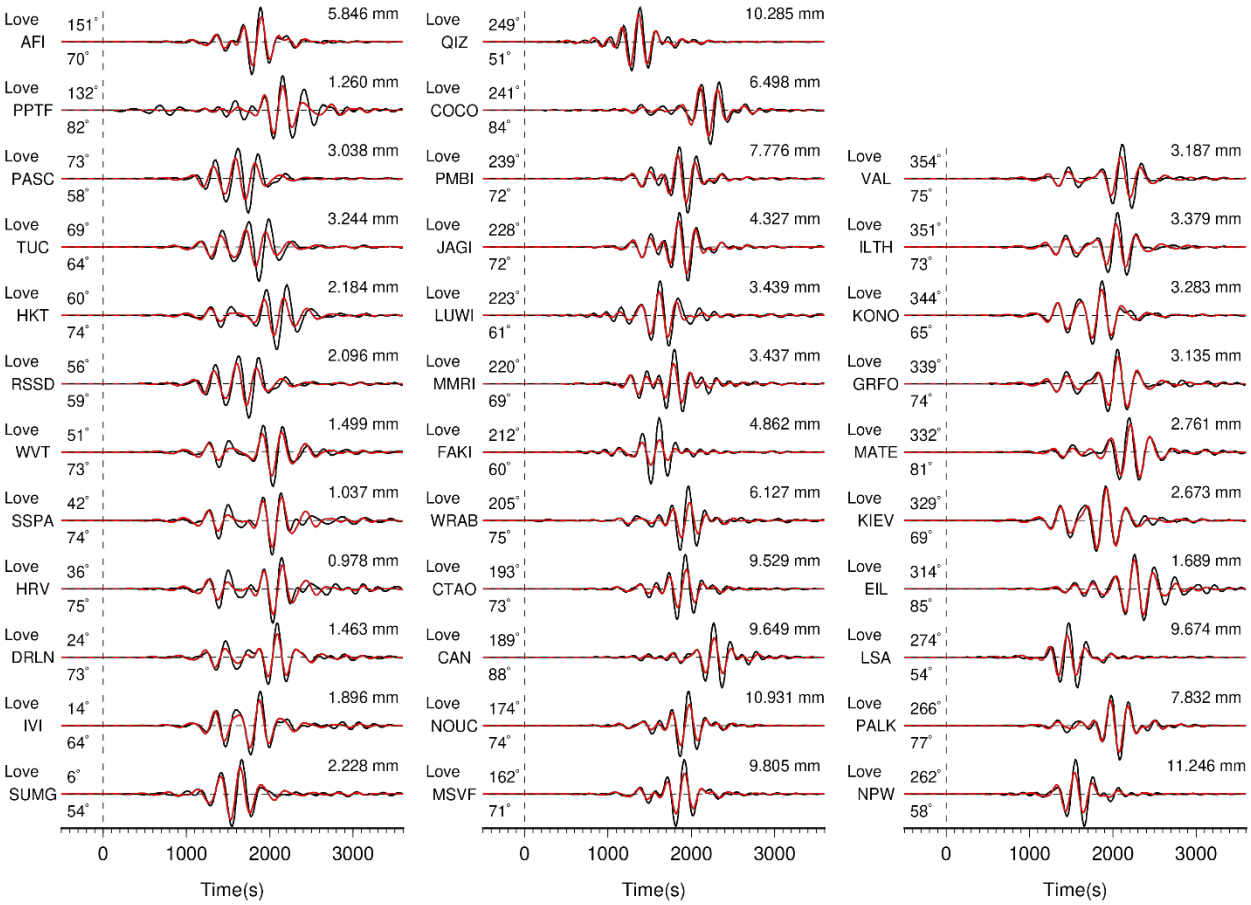

Fig. S6. Comparison between observed teleseismic long-period Love wave ground displacement waveforms (black lines) and synthetic seismograms (red lines) generated by Model I shown in fig. S3A. The wave type and the station name are shown at the top of each trace, along with azimuth and epicentral distance in degrees.

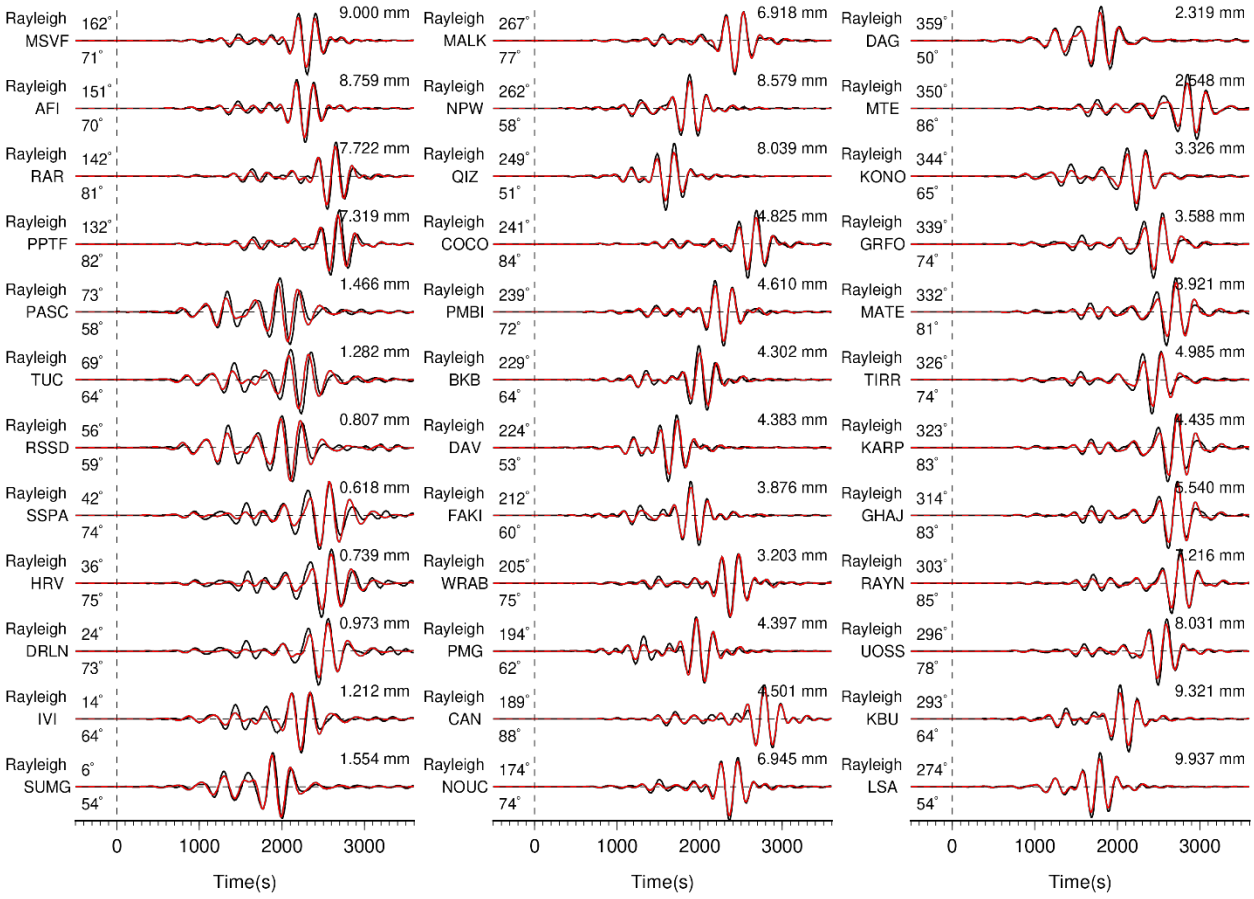

Fig. S6. Continued, for Rayleigh waves.

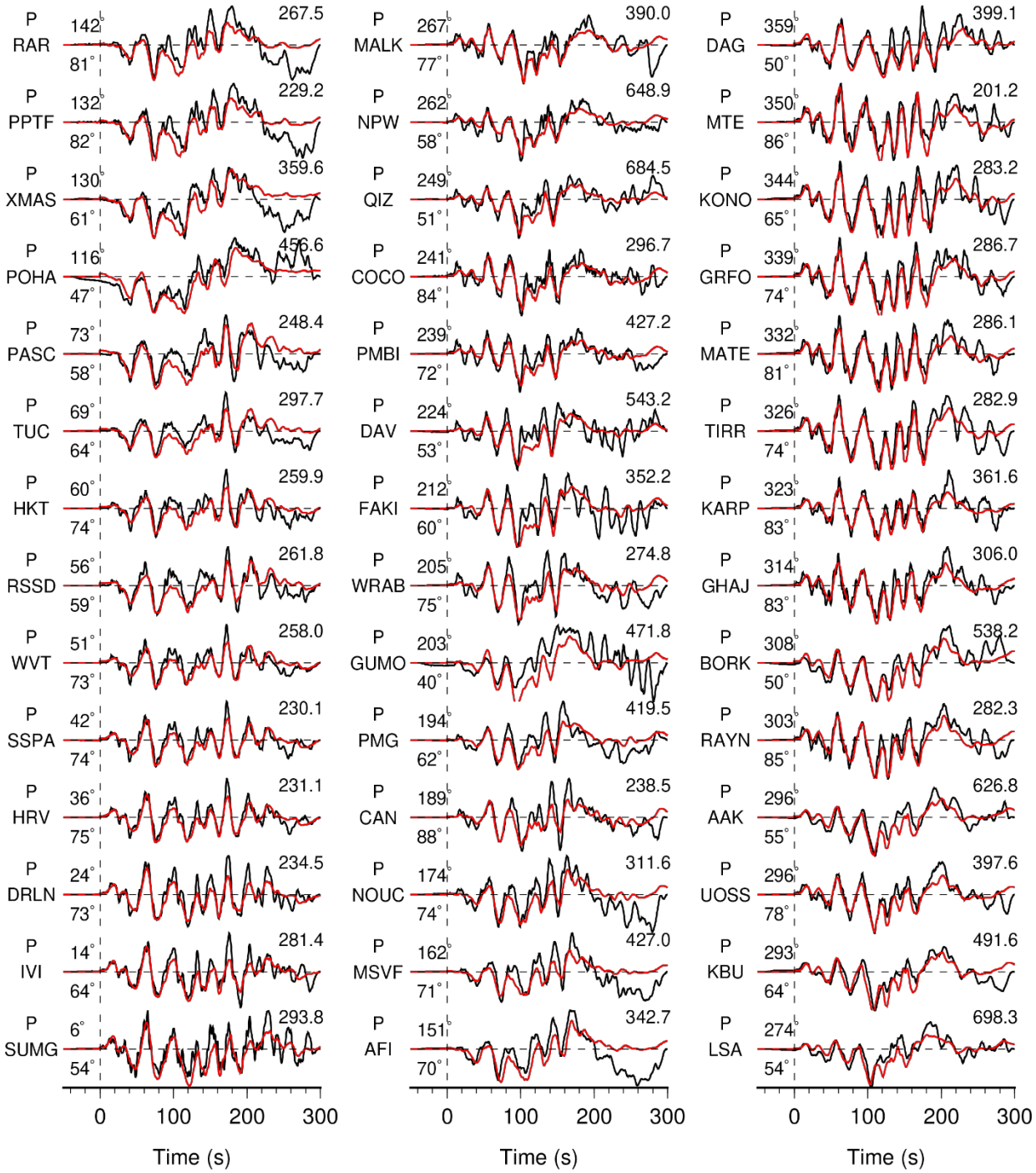

Fig. S7. Comparison of observed (black) and synthetic (red) teleseismic *P* wave ground displacements for the Model II shown in fig. S3B. Data and synthetic seismograms are manually aligned on the first arrivals. Station names and phase-type are indicated on the left of each comparison. The azimuth (above) and epicentral distance (below) in degrees are shown at the beginning of each record. The number above the right portion of each comparison is the peak amplitude of the observed ground displacement in μm.

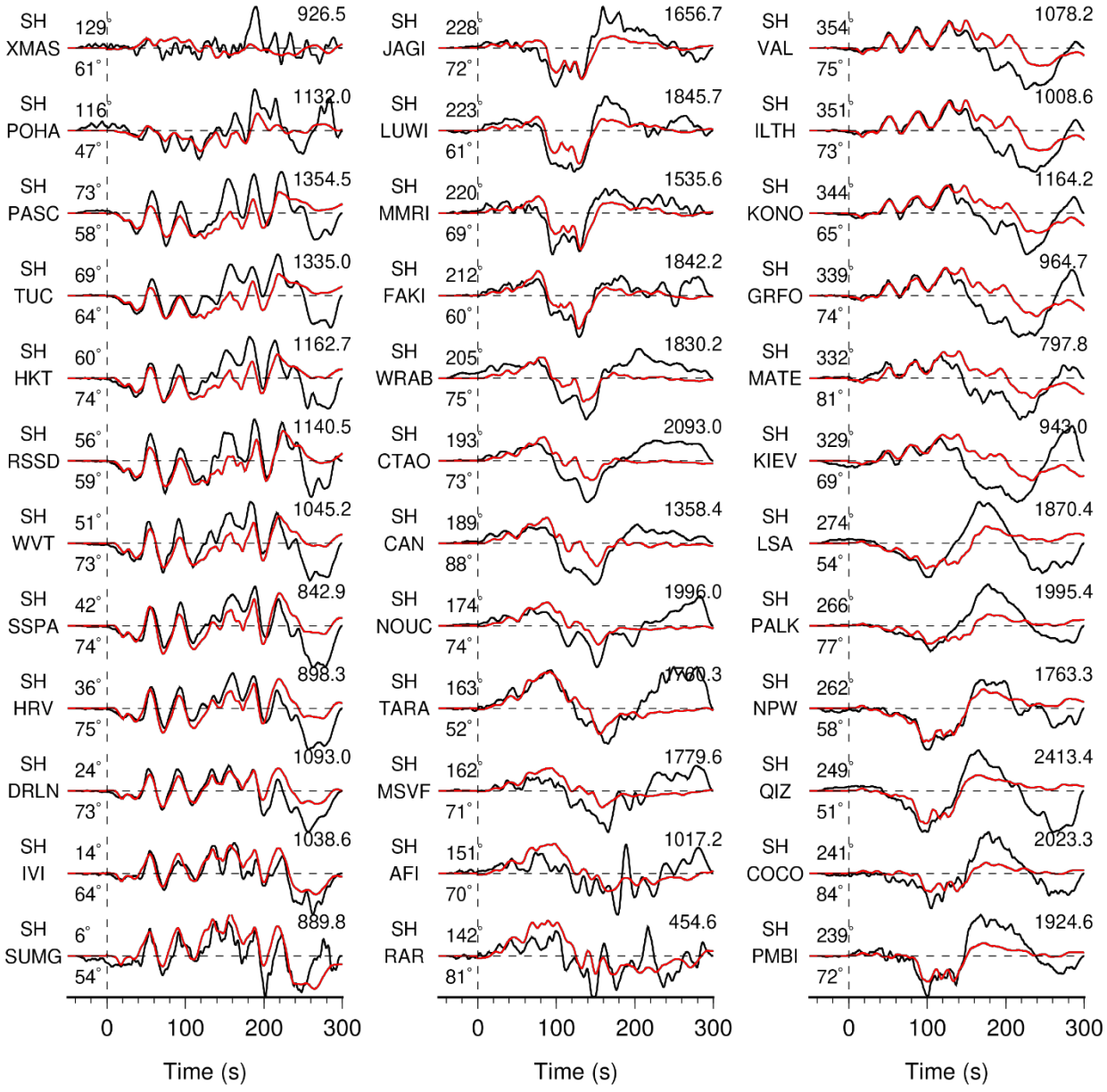

Fig. S7. Continued, for *SH* waves.

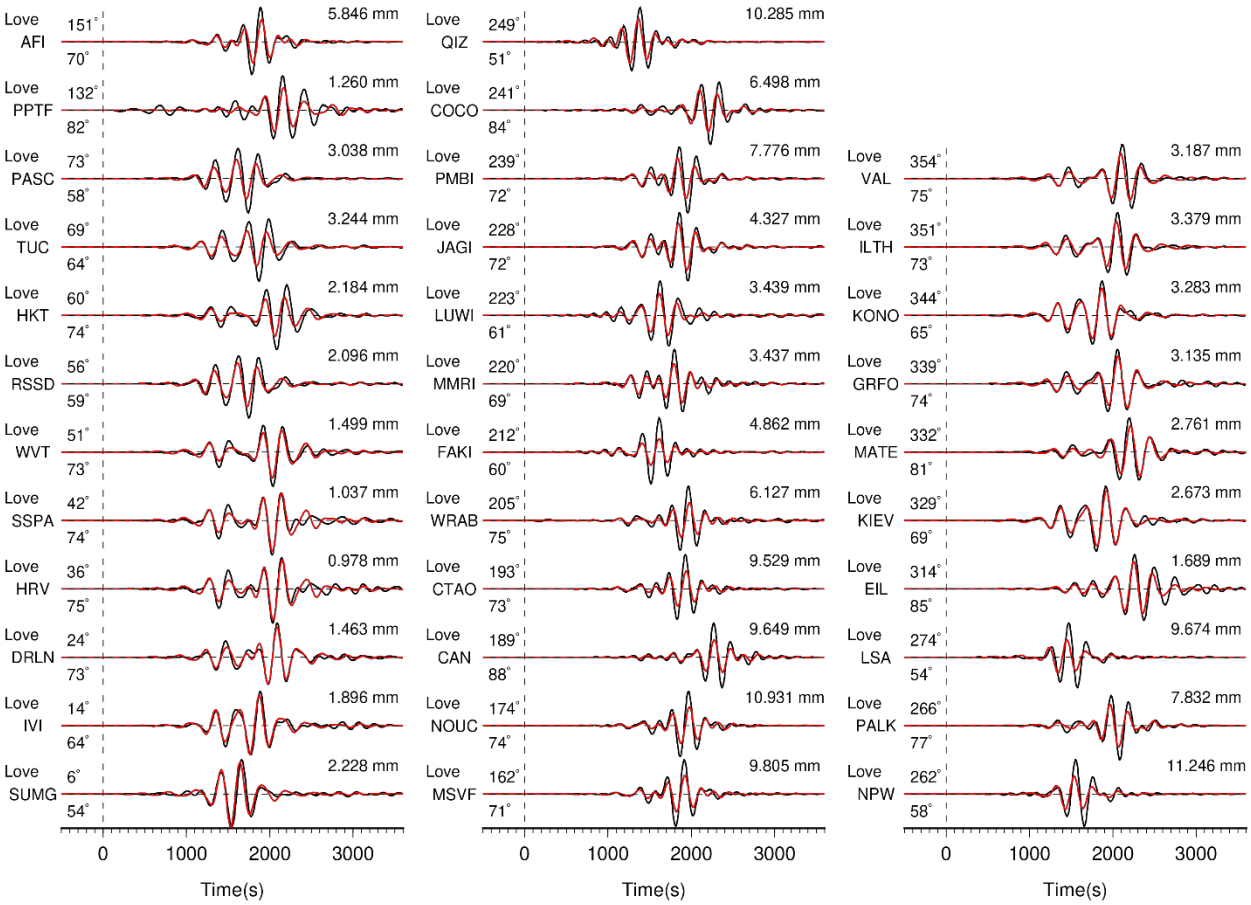

Fig. S8. Comparison between observed teleseismic long-period Love wave ground displacement waveforms (black lines) and synthetic seismograms (red lines) generated by Model II shown in fig. S3B. The wave type and the station name are shown at the top of each trace, along with azimuth and epicentral distance in degrees.

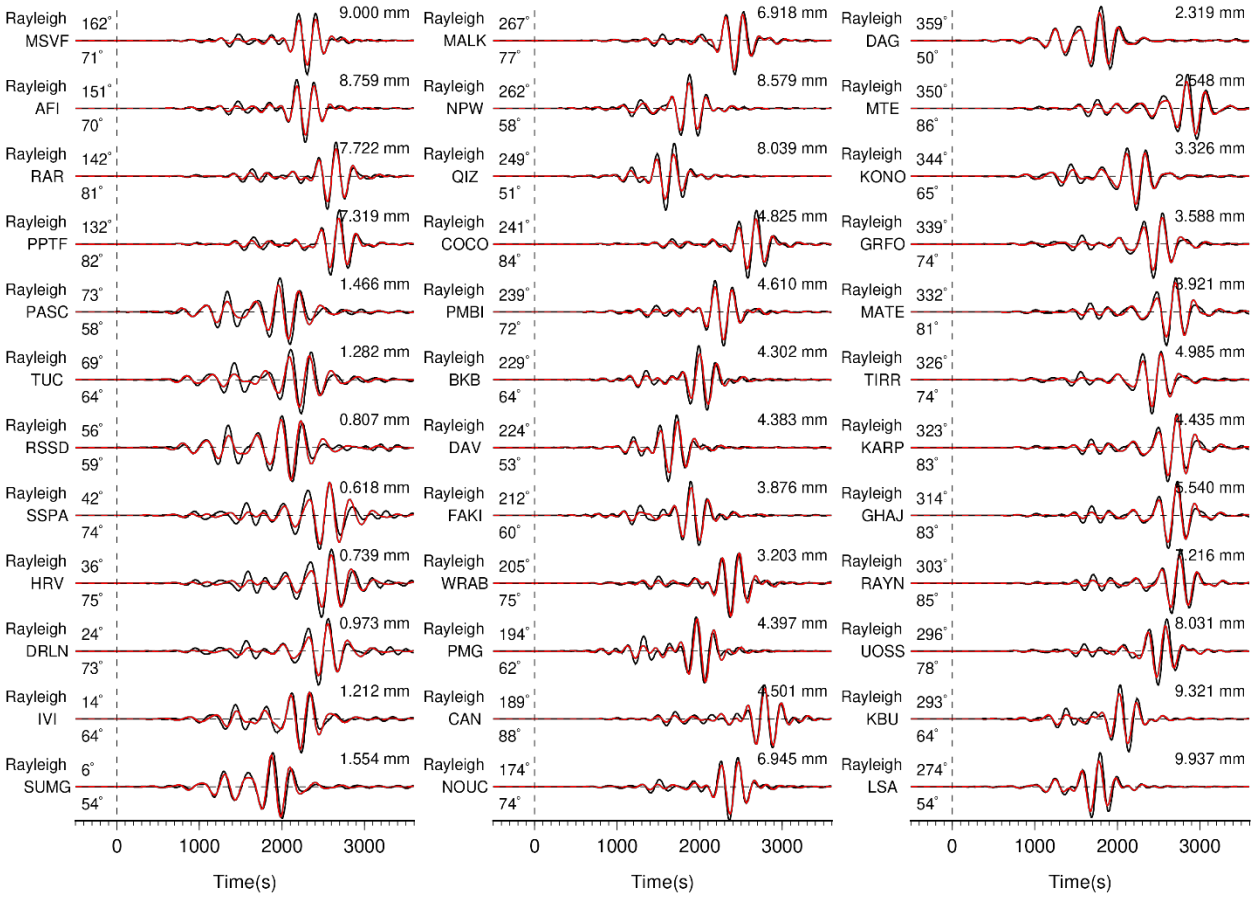

Fig. S8. Continued, for Rayleigh waves.

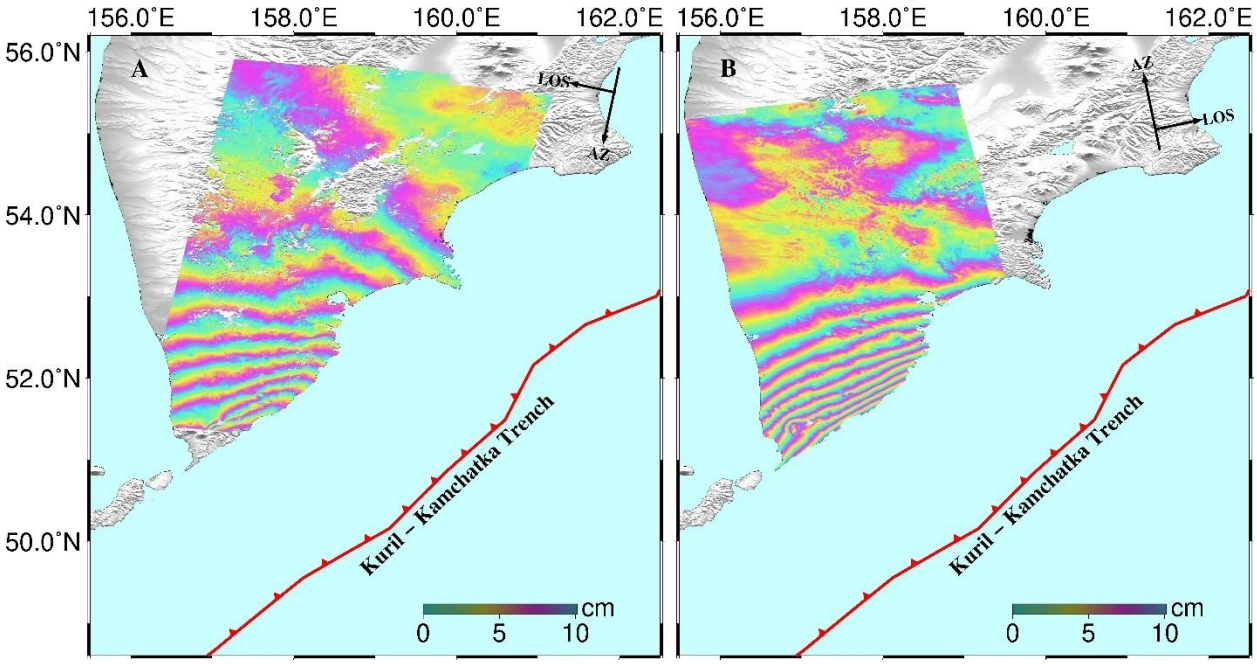

Fig. S9. Coseismic interferograms for the 2025 *Mw* 8.8 Kamchatka event. (A) and (B) show the coseismic interferograms from the descending Sentinel-1 track T060 and the ascending track T111, respectively. Arrows indicate the satellite trajectory and line-of site for the interferograms.

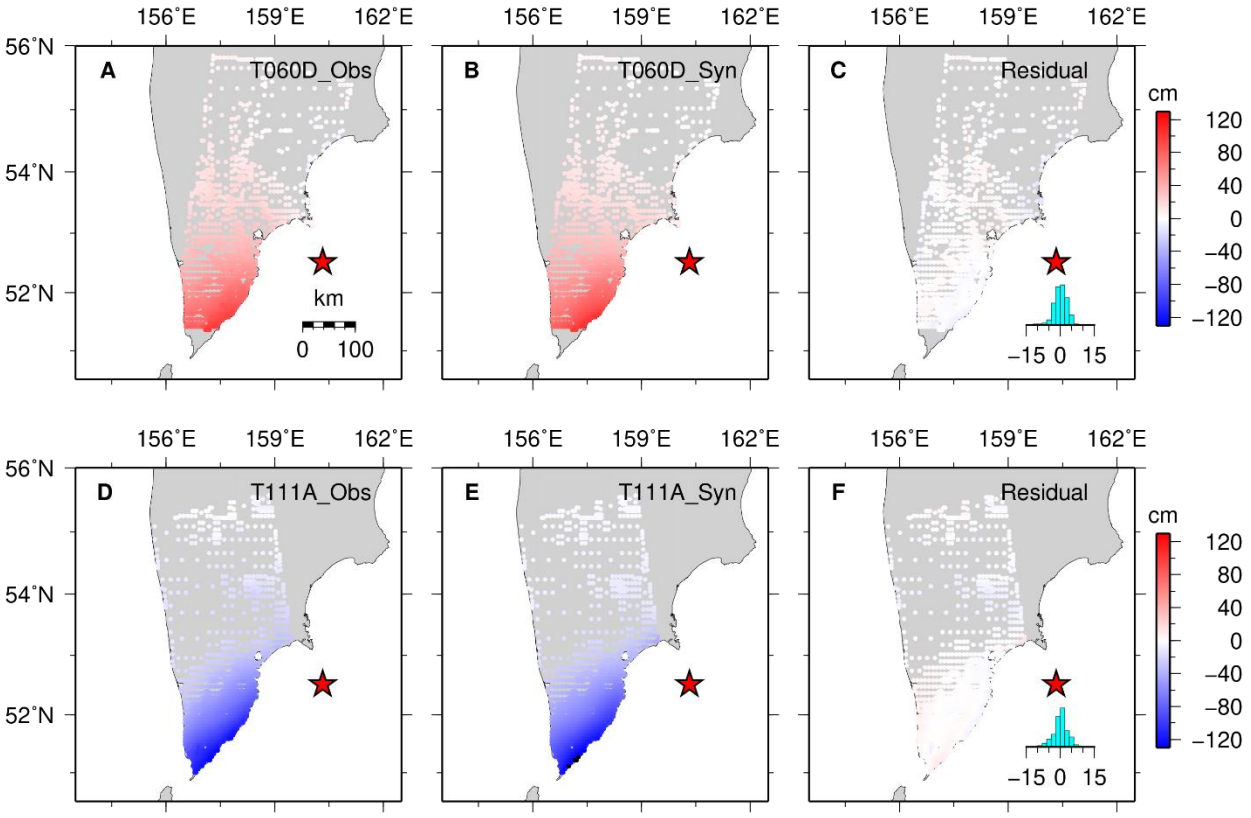

Fig. S10. Comparison of the observed InSAR displacements and predictions for Model III in Fig. 2A. (A) and (D) show the unwrapped LOS displacements of the descending track T060 and ascending tracks T111, respectively. (B) and (E) indicate the corresponding predictions from the Model III. (C) and (F) show residuals along the ascending and descending paths, respectively.

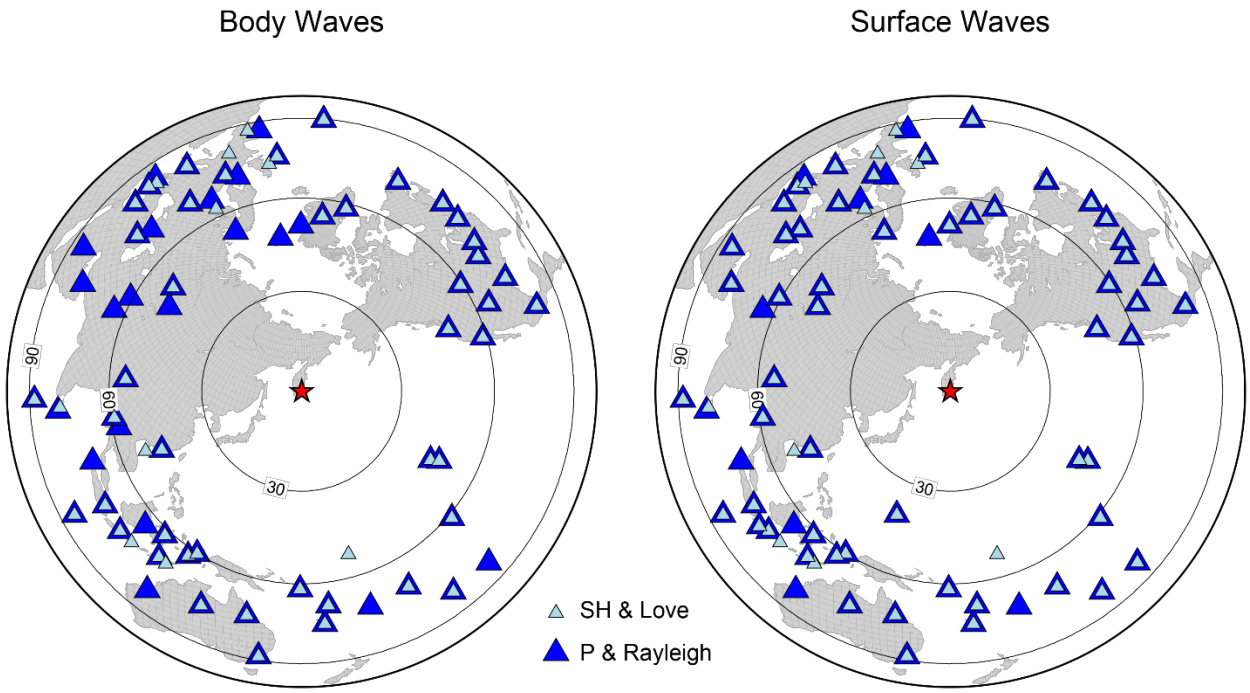

Fig. S11. Distributions of the expanded number of teleseismic broadband stations providing body-wave (left) and surface-wave (right) ground displacement observations used in the inversions for Model III.

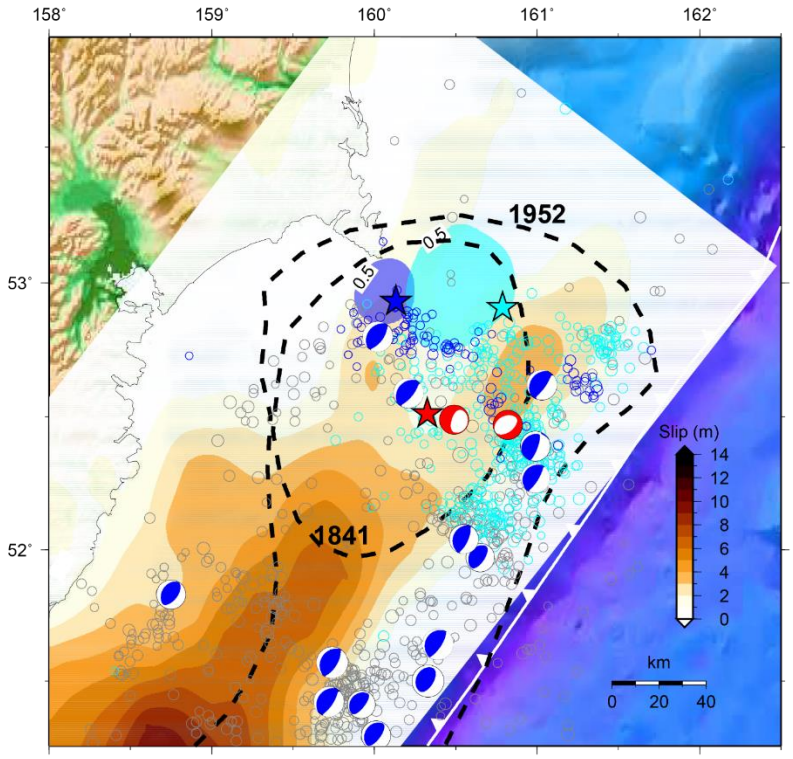

Fig. S12. Surface projection of slip in Model III near the epicentral region. Dashed contours delineate the historical rupture zones of the 1841 and 1952 earthquakes. Focal mechanisms are GCMT solutions, scaled by moment magnitude. Blue circles and the blue star represent the aftershocks and epicenter of the 17 August 2024 M_W 7.0 earthquake, respectively. Cyan circles and the cyan star represent the aftershocks and epicenter of the 20 July 2025 M_W 7.4 earthquake, respectively. The USGS-NEIC slip distributions (≥0.5 m) for the 2024 M_W 7.0 and 2025 M_W 7.4 events are shown as transparent blue and cyan patches, respectively.

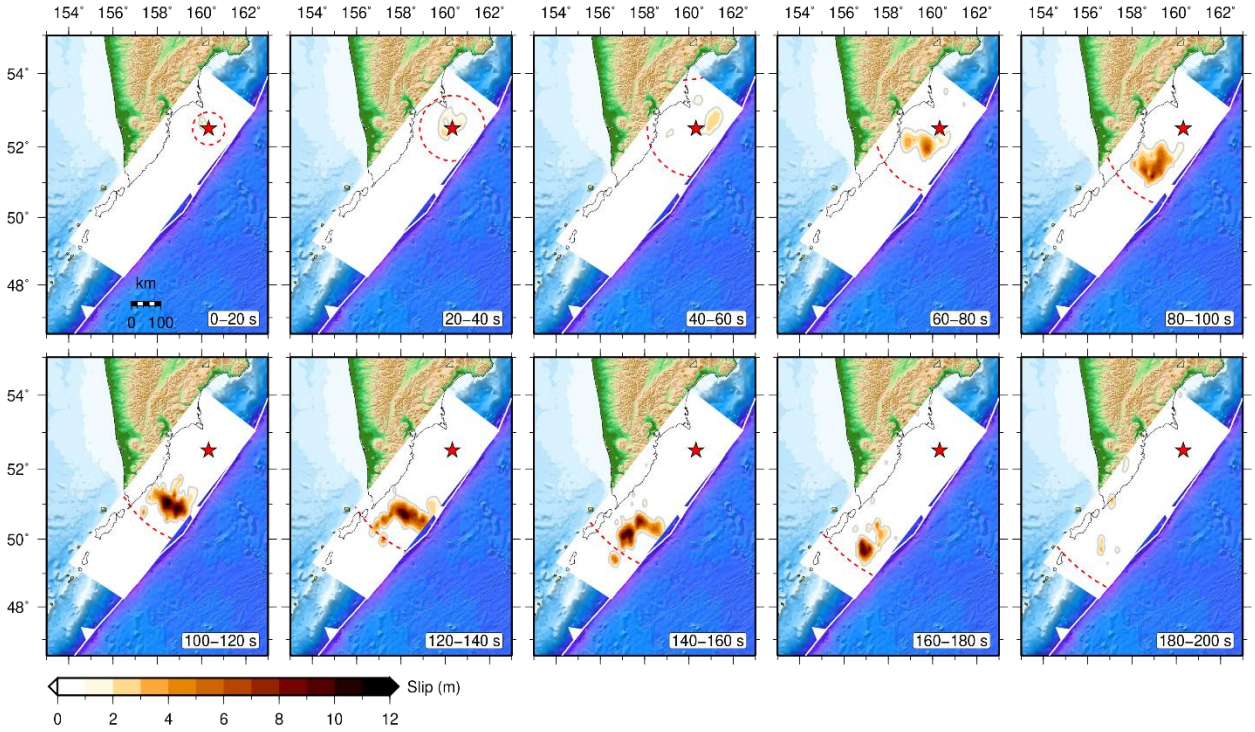

Fig. S13. Snapshots of the rupture history for Model III of the 29 July 2025 M_W 8.8 Kamchatka earthquake with a time interval of 20 s. The red dashed contour denotes the position of a reference rupture front with a rupture velocity of 2.5 km/s, and colors indicate the slip magnitude.

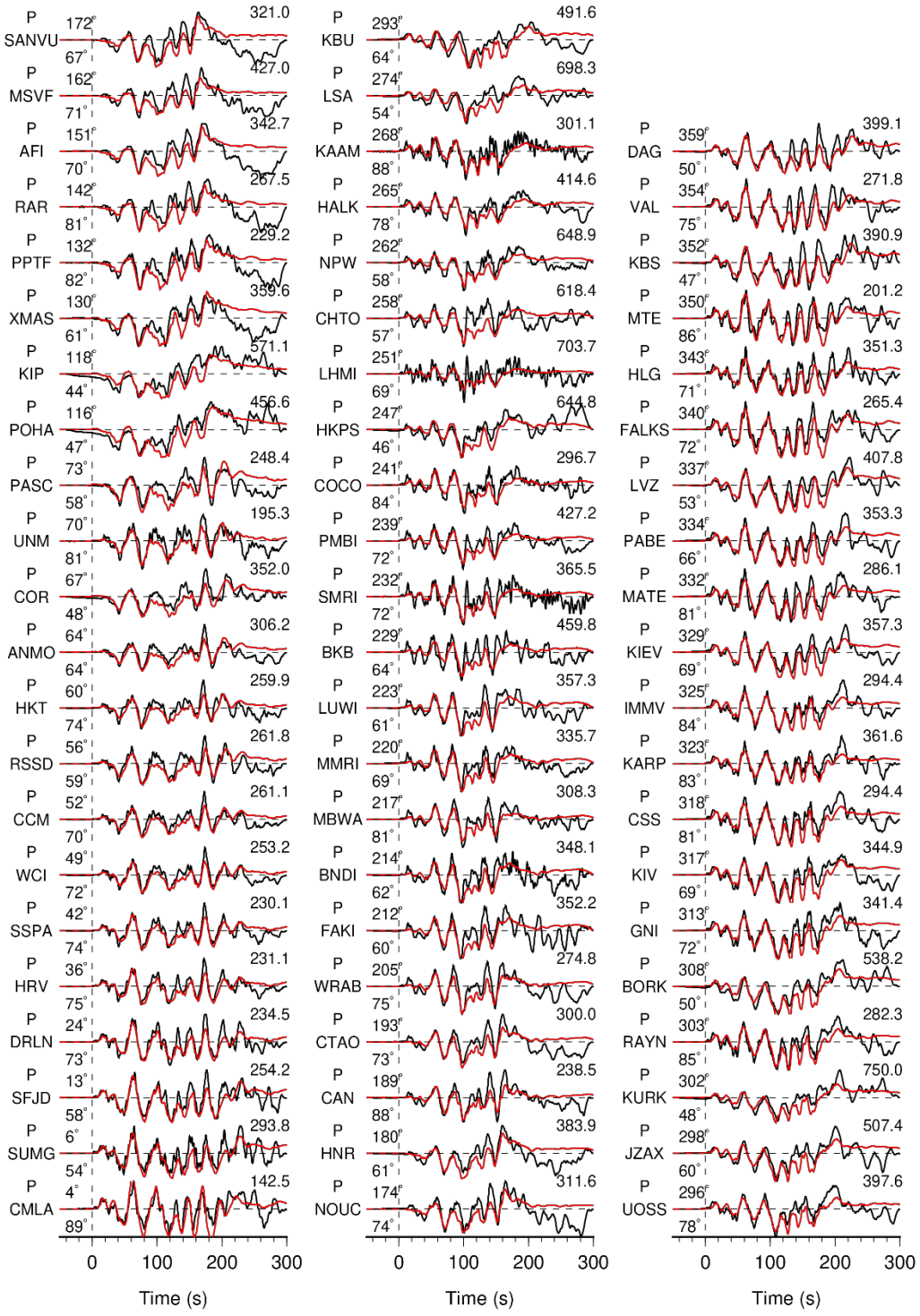

Fig. S14. Comparison of observed (black) and synthetic (red) teleseismic *P* wave ground displacements for Model III shown in Fig. 2A. Data and synthetic seismograms are manually aligned on the first arrivals. Station names and phase-type are indicated on the left of each comparison. The azimuth (above) and epicentral distance (below) in degrees are shown at the beginning of each record. The number above the right portion of each comparison is the peak amplitude of the observed ground displacement in μm.

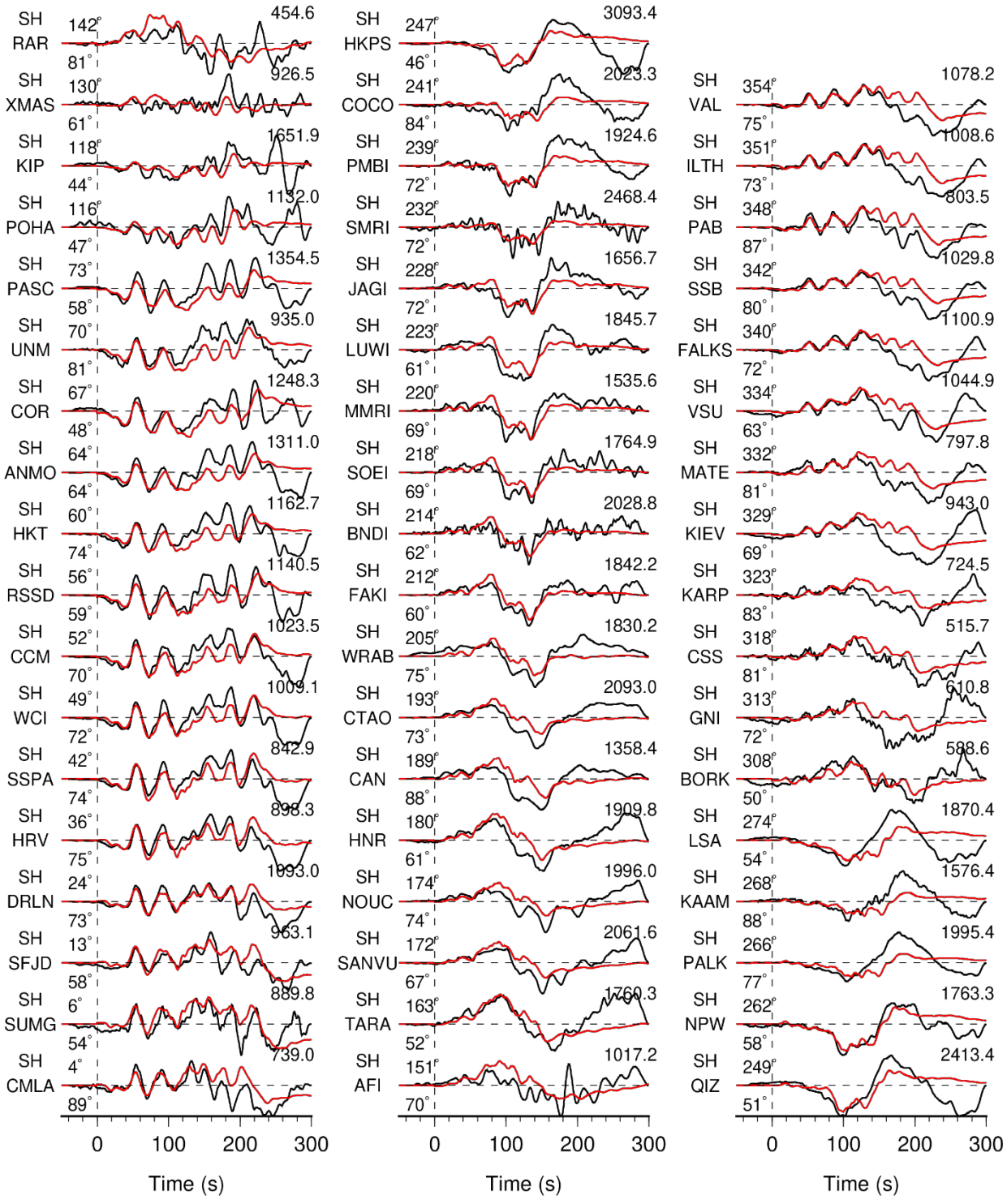

Fig. S14. Continued, for *SH* waves

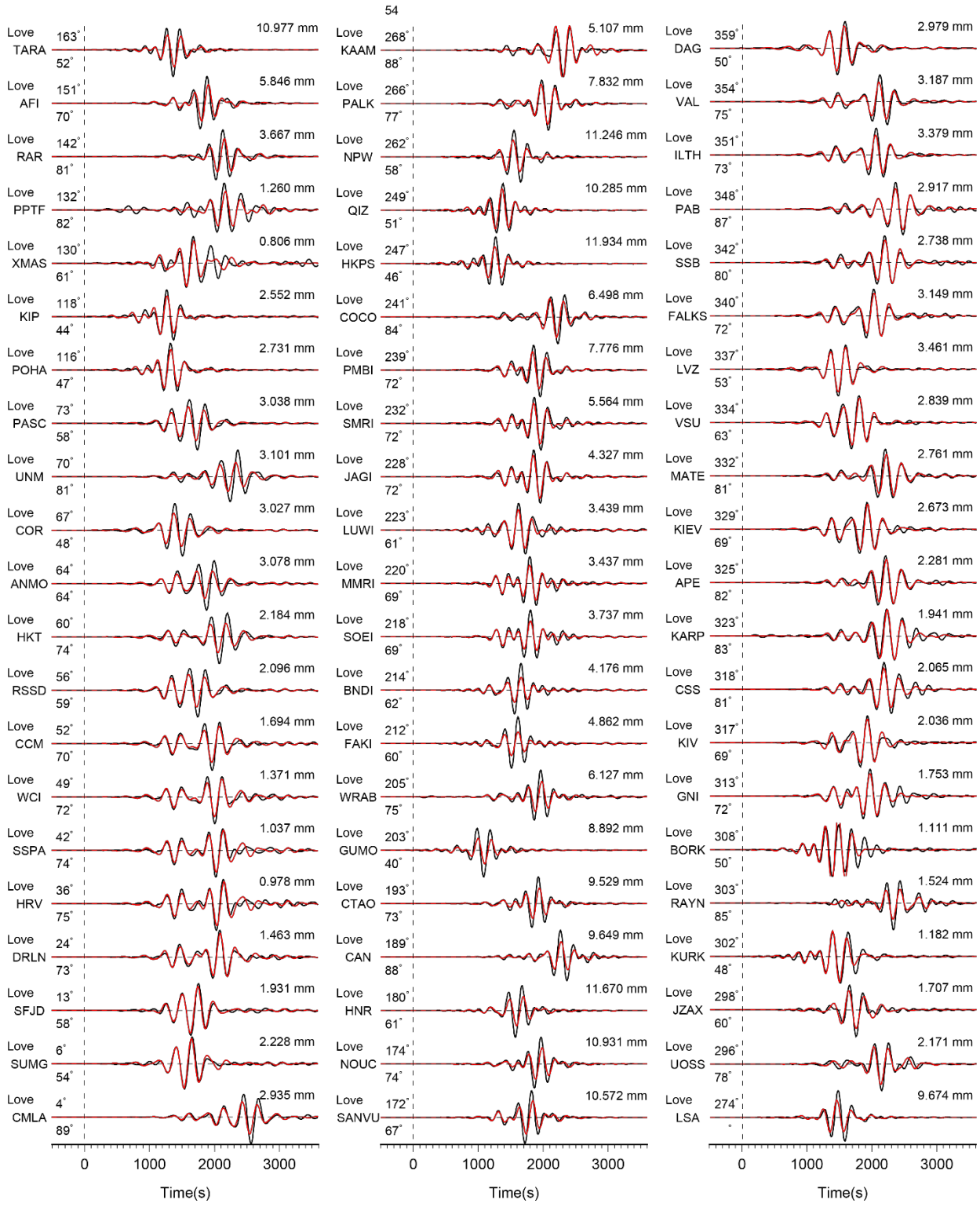

Fig. S15. Comparison between observed teleseismic long-period Love wave waveforms (black lines) and synthetic seismograms (red lines) generated by Model III shown in Fig. 2A. The wave type and the station name are shown at the top of each trace, along with azimuth and epicentral distance in degree.

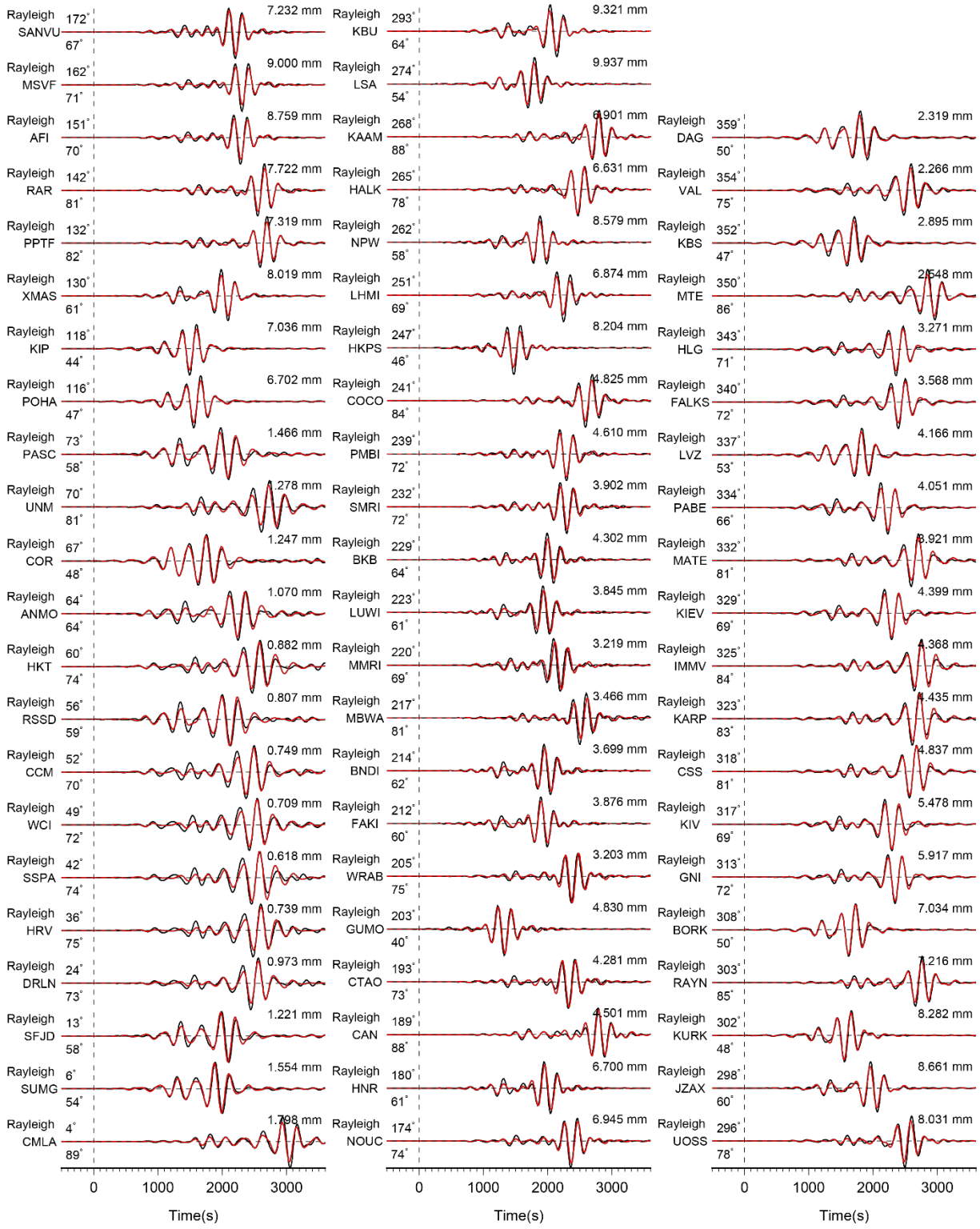

Fig. S15. Continued, for Rayleigh waves.

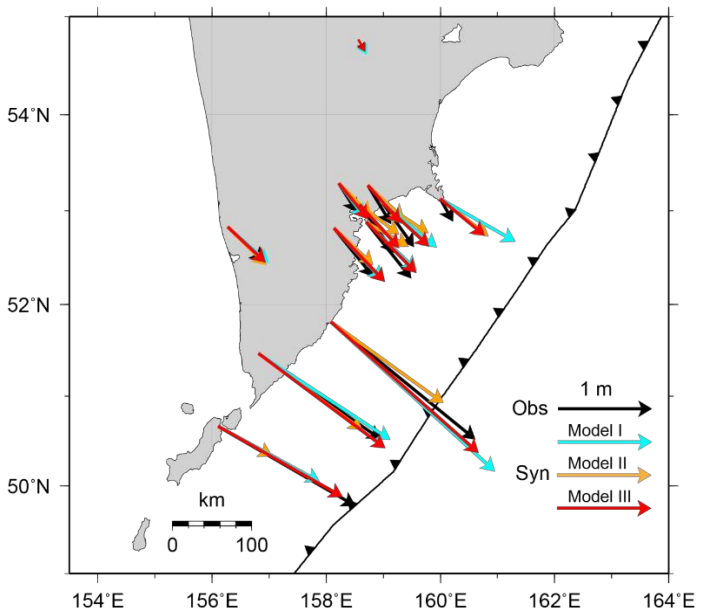

Fig. S16. Comparison between digitized observed (black) and computed static GNSS displacements for the slip models shown in fig. S3A (cyan), fig. S3B (orange), and Fig. 2A (red).

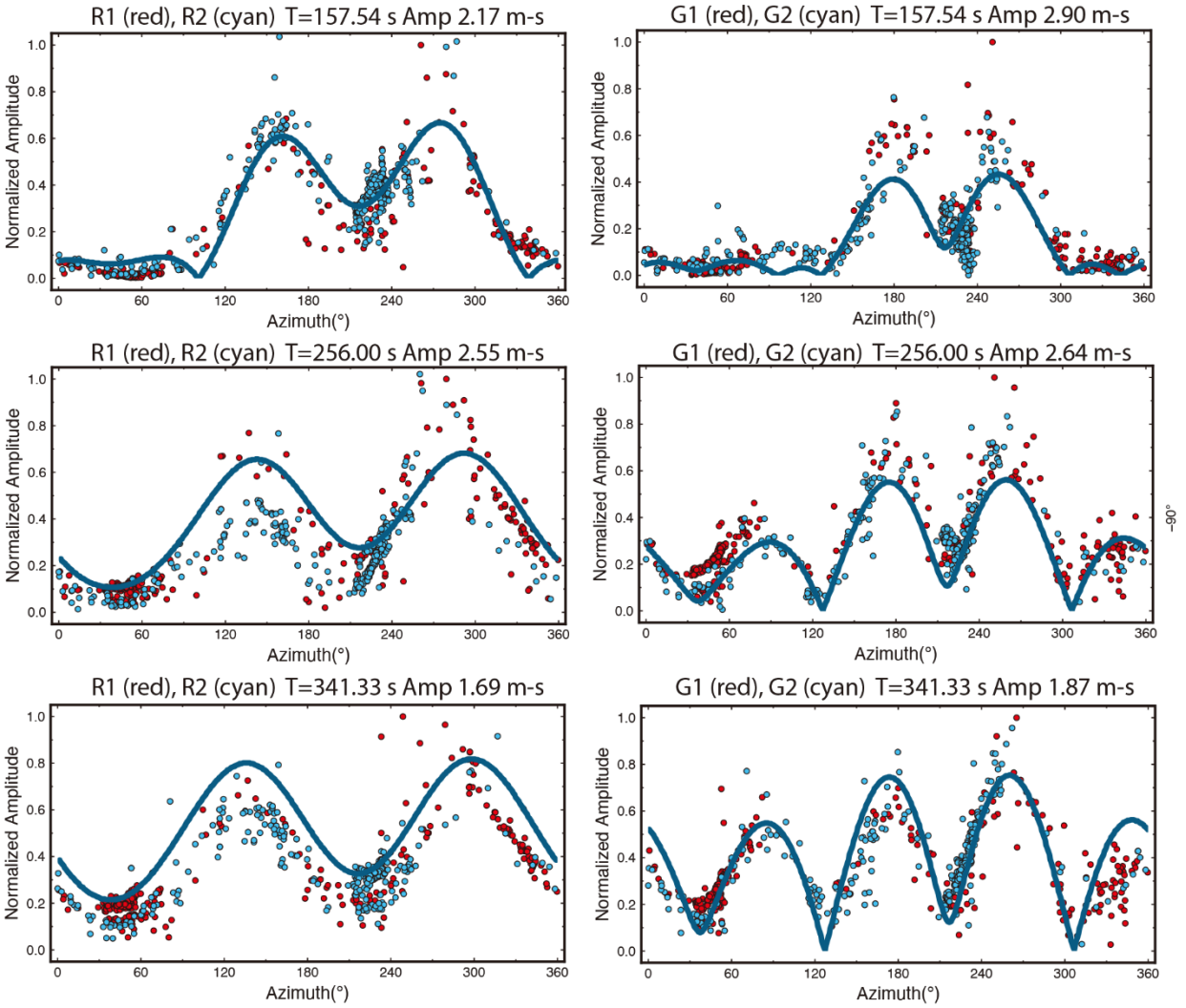

Fig. S17. Long-period surface wave spectral amplitudes. Long period Rayleigh wave short-arc (R1) and long-arc (R2) spectra for periods of 157.54, 256.00, and 341.33 s are shown versus azimuth on the left column and Love wave short-arc (G1) and long-arc (G2) spectra for the same periods are shown on the right column. Group velocity windows were used to isolate the phases and the spectra were corrected for propagation distance and attenuation back to the source. For a shallow thrust event with no spatial finiteness, the Rayleigh wave pattern should be symmetric with two lobes and the Love wave pattern should have four lobes. Finiteness of the source modifies the effective radiation pattern, with unilateral southwestward rupture causing deviations from the point-source expectations. This is demonstrated by the blue curves, which are for a unilateral line-source rupture with azimuth 220° and rupture velocity 2.44 km/s with uniform slip along 300 km of the plate boundary, a rise time of 40 s, and focal mechanism given by the average value for Model III in Fig. 2A. This simple model approximates the favored slip Model III, and accounts for the observed period dependent-change in both the Rayleigh and Love wave spectra well, demonstrating the simplicity of the source rupture.

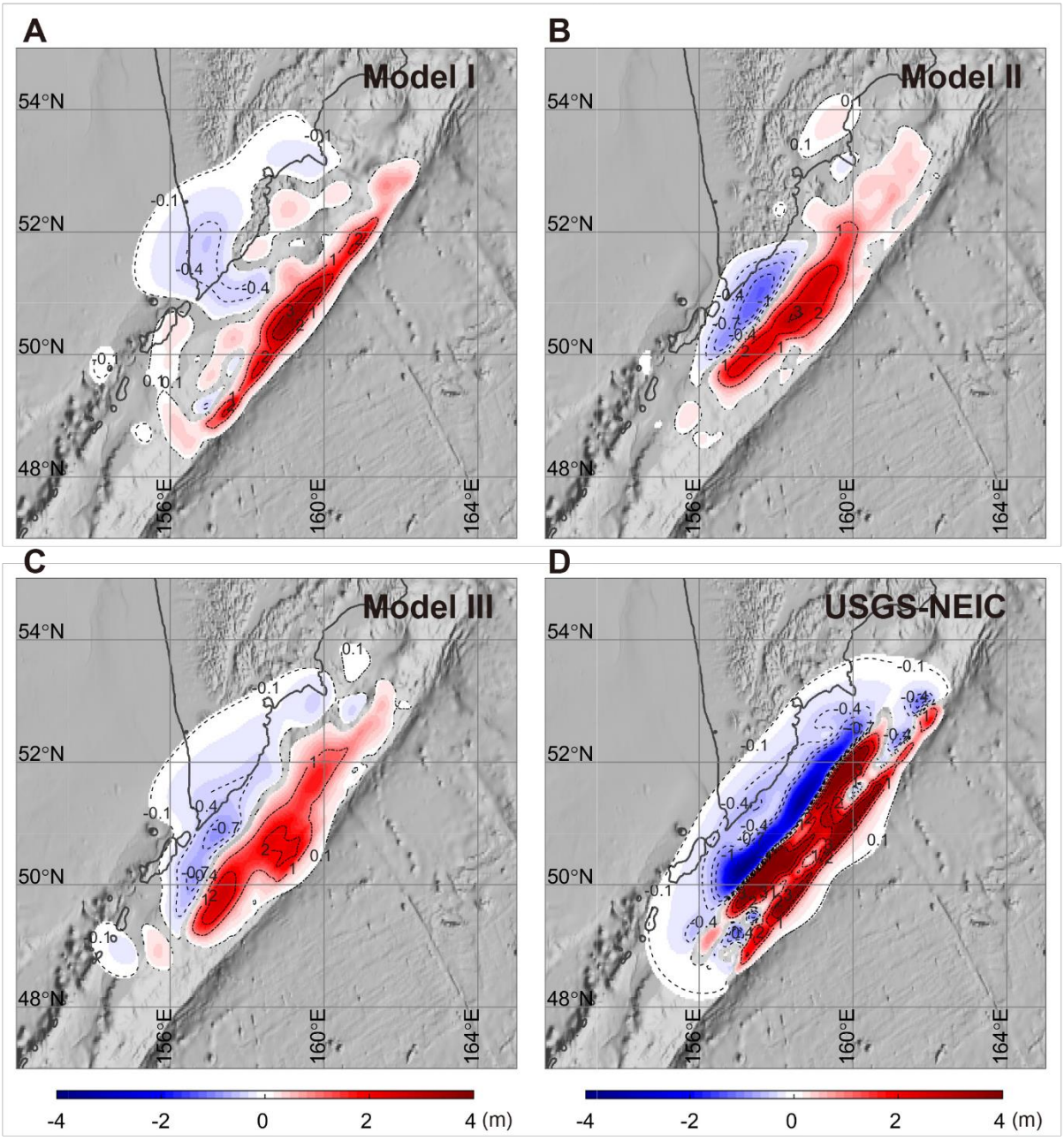

Fig. S18. Vertical seafloor and land surface deformation computed from Model I (A), Model II (B), Model III (C), and the USGS-NEIC model (D), respectively.

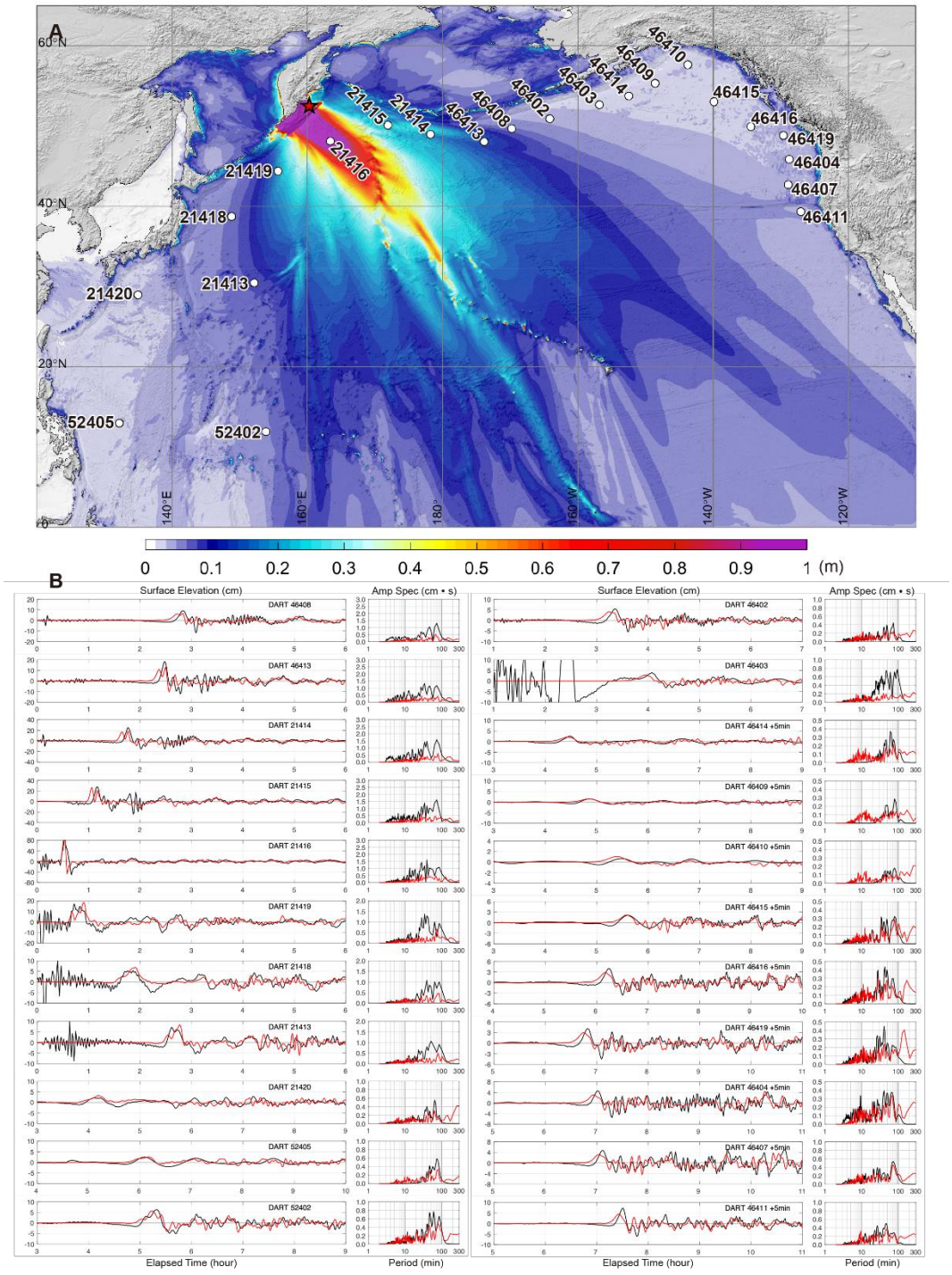

Fig. S19. Similar to Fig. 3, but showing maximum sea surface elevation map (A) and comparison of tsunami waveforms and predictions for Model I shown in fig. S3A (B). Black lines indicate the observed time series (left) and amplitude spectra (right), while red lines represent the predictions.

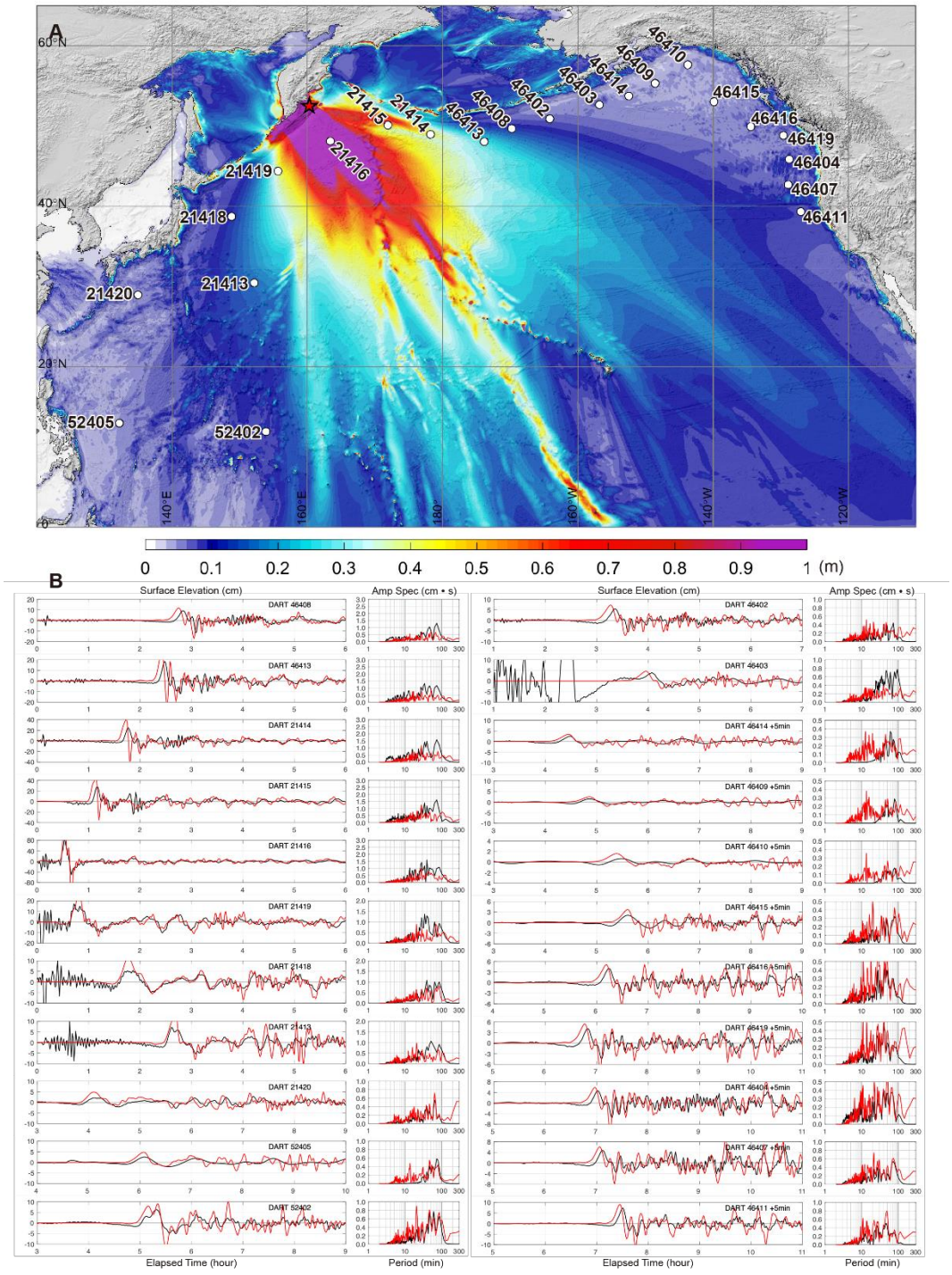

Fig. S20. Similar to Fig. 3, but showing maximum sea surface elevation map (A) and comparison of tsunami waveforms and predictions for the USGS-NEIC three-segment model shown in fig. S3C (B). Black lines indicate the observed time series (left) and amplitude spectra (right), while red lines represent the predictions.

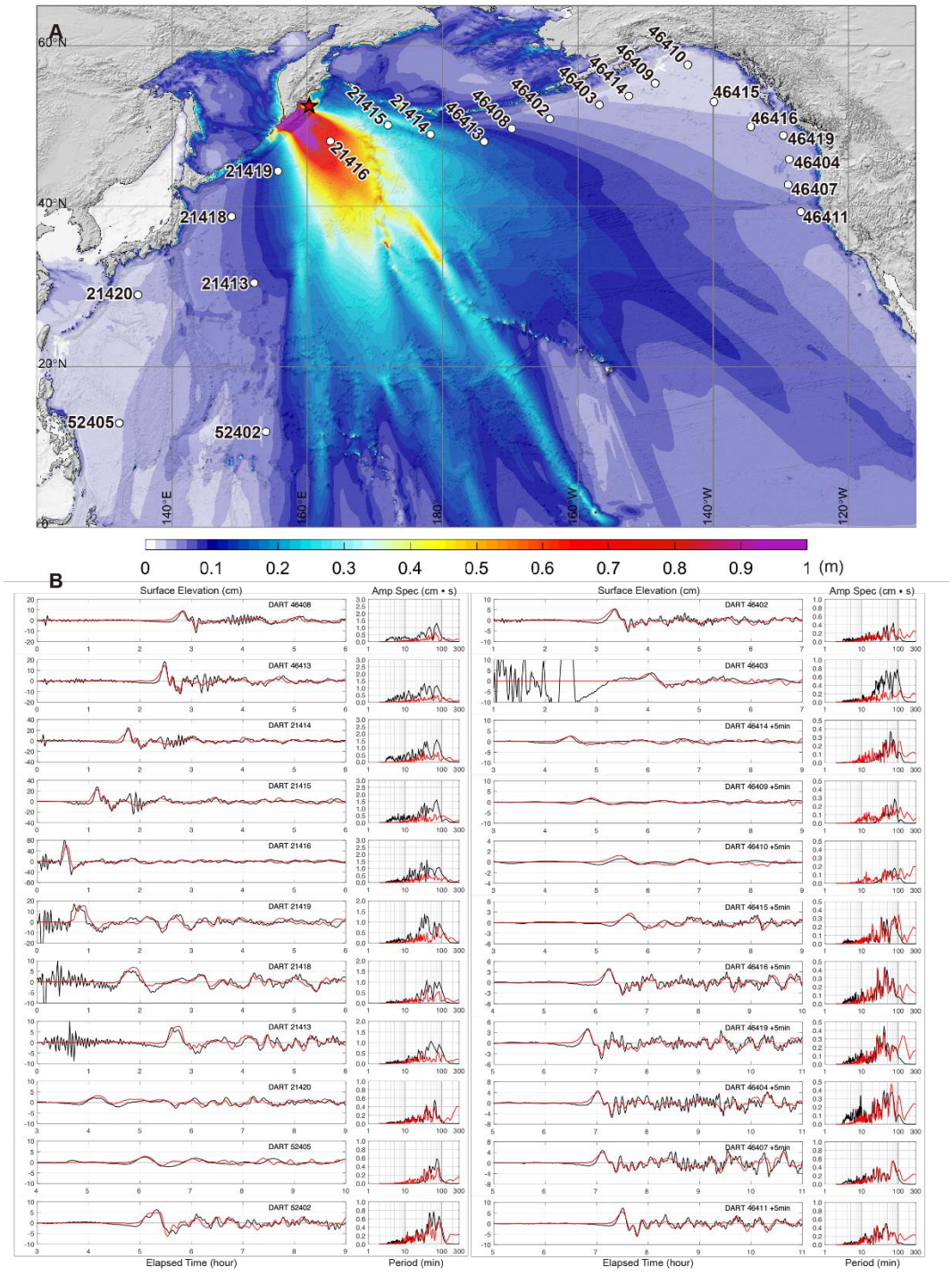

Fig. S21. Similar to Fig. 3, but showing maximum sea surface elevation map (A) and comparison of tsunami waveforms and predictions for Model II shown in fig. S3B (B). Black lines indicate the observed time series (left) and amplitude spectra (right), while red lines represent the predictions.

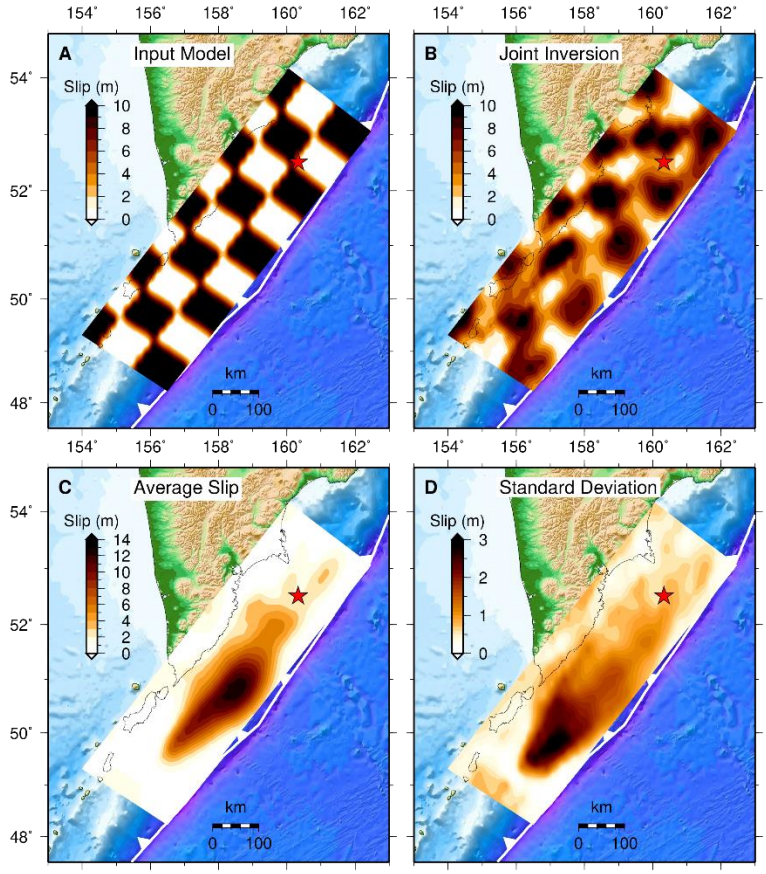

Fig. S22. Resolution test and model uncertainties. (A) Input slip model used to generate the synthetic data sets. (B) Inverted slip model obtained from these synthetic data. (C) Mean slip distribution from 50 plausible solutions, each derived using a different random seed. (D) Standard deviation of the slip distribution among the 50 plausible models.

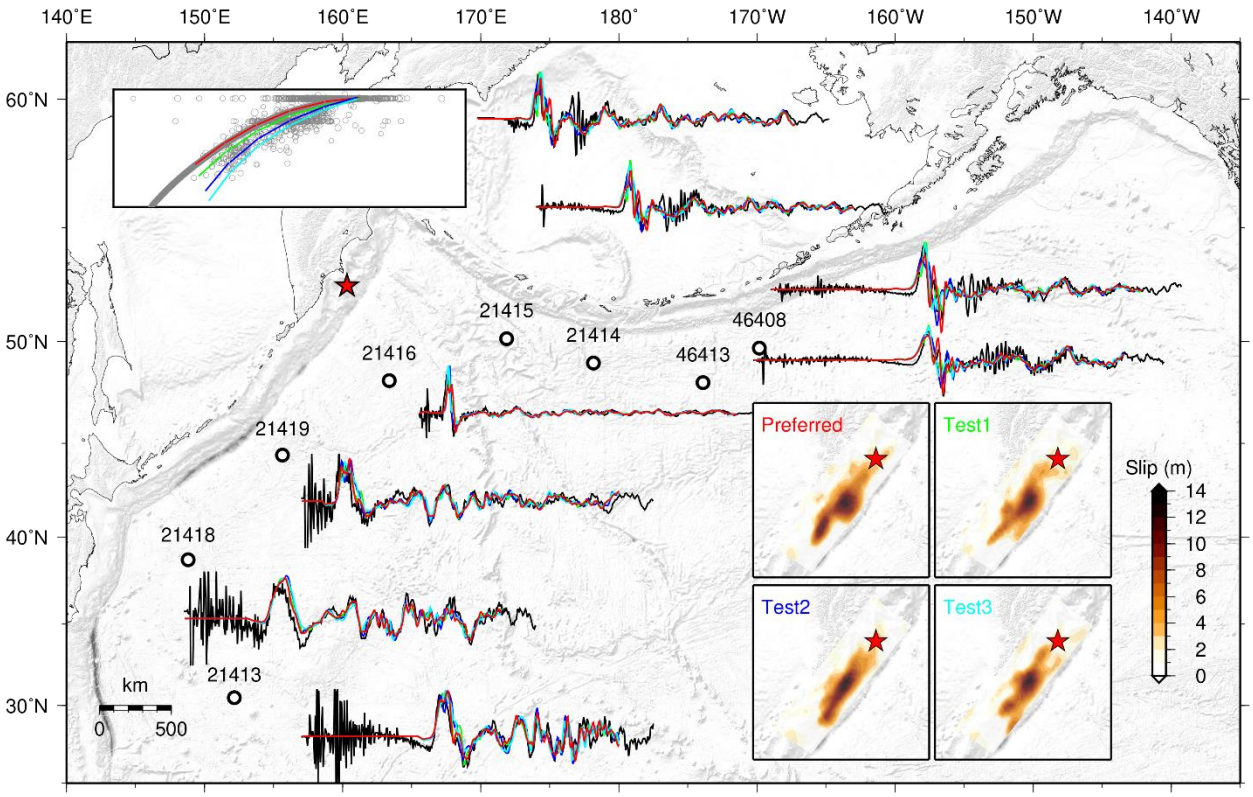

Fig. S23. Comparison of tsunami waveforms predicted by the preferred model (Model III) and the test models with alternative fault geometries.

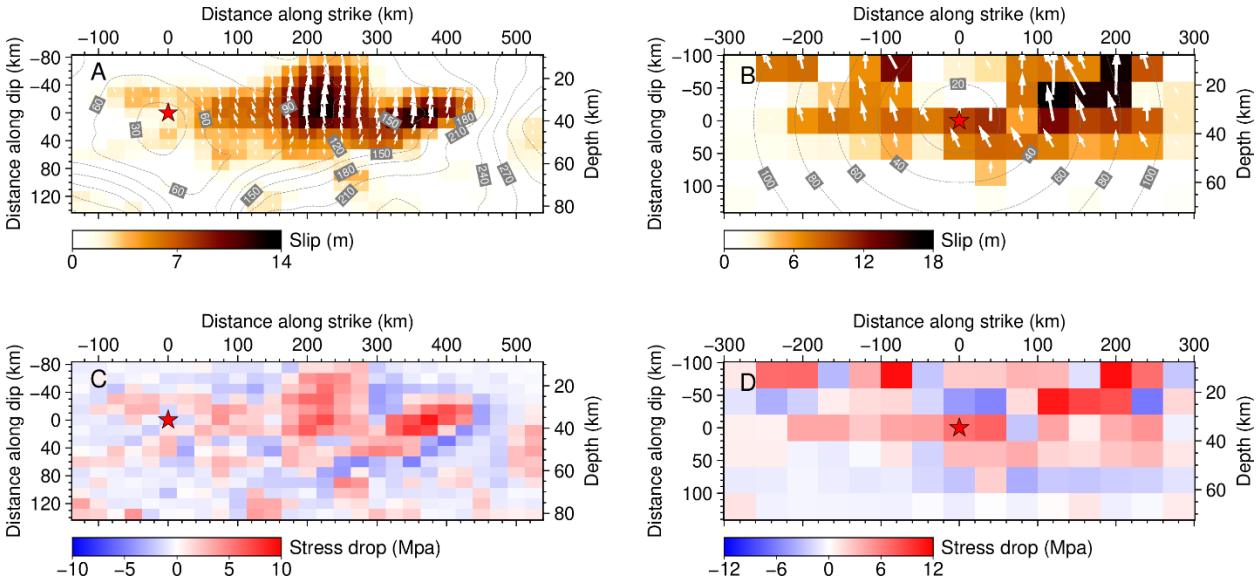

Fig. S24. Comparison of the preferred slip models for the 2025 M_W 8.8 Kamchatka earthquake (A) and the 2010 Maule M_W 8.8 earthquake (B) (*32*). (C) and (D) Corresponding static stress drops, calculated following the method of (*86*).

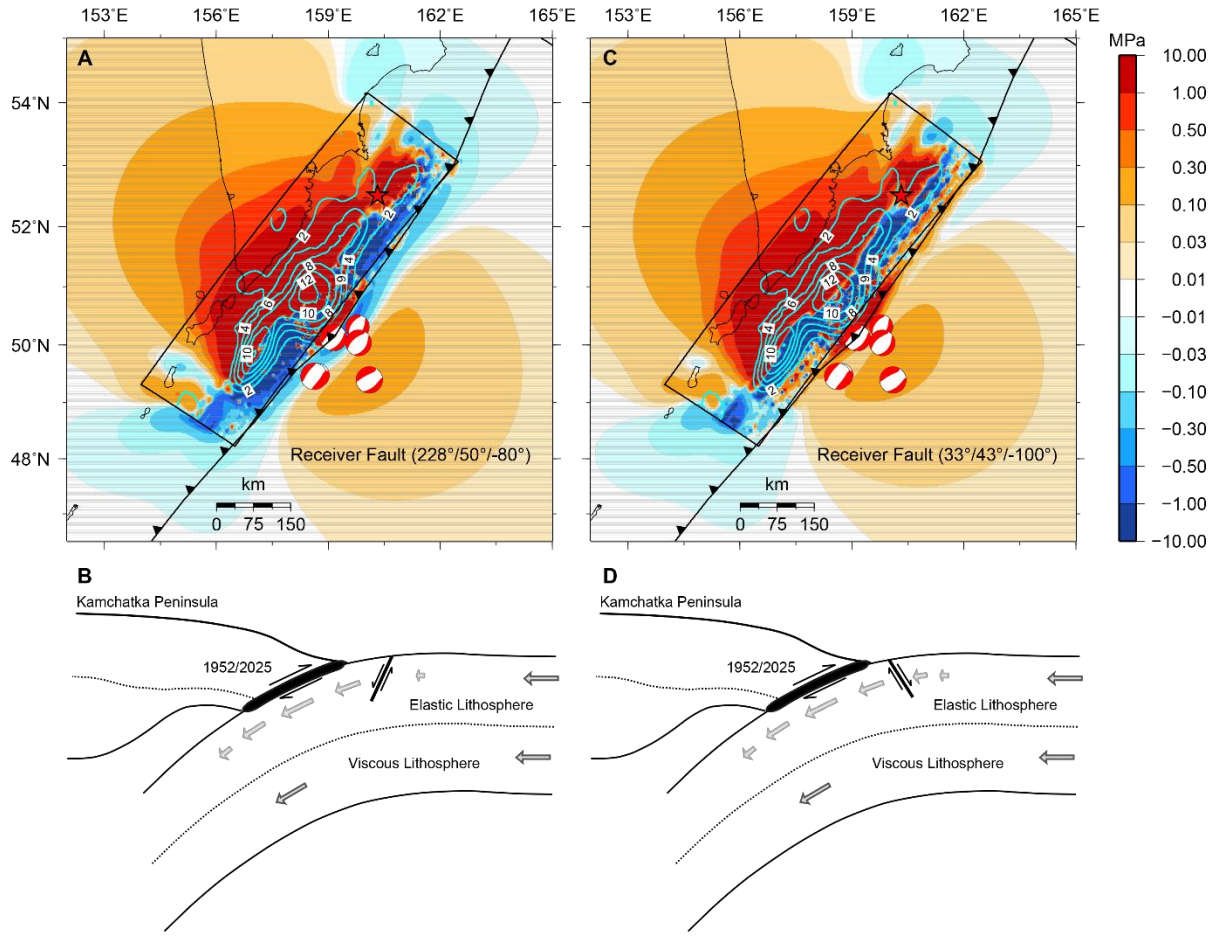

Fig. S25. Maps of Coulomb stress changes induced by the 2025 M_W 8.5 Kamchatka earthquake for outer–rise normal fault geometries. (A) and (C) Coulomb stress change averaged over depths of 10–16 km on different receiver faults. (B) and (D) Corresponding schematic cross–sections indicating the target fault geometries.

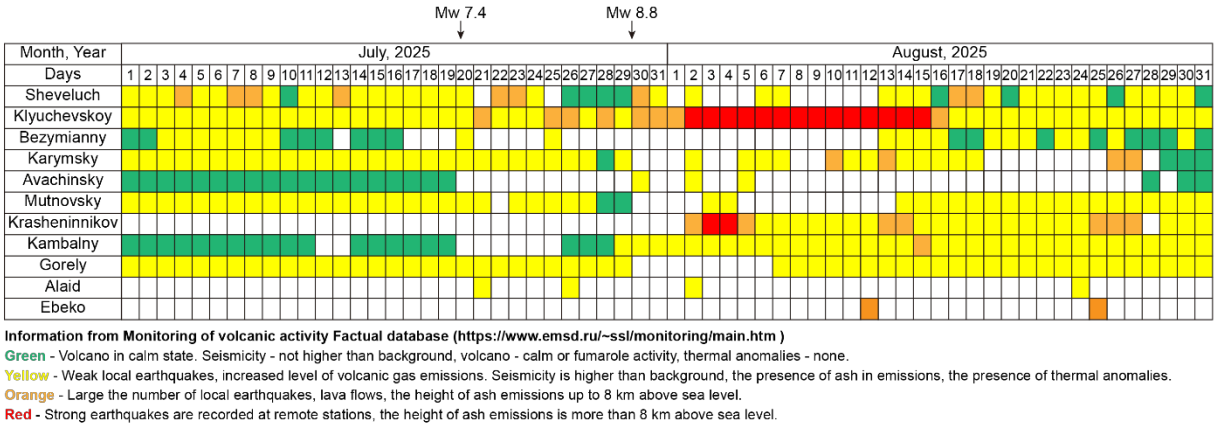

Fig. S26. A daily timeline of volcanic activities of 11 closely monitored volcanoes in Kamchatka occurring before and after the M_W 7.4 foreshock and M_W 8.8 mainshock. Some volcanoes appear to have increased activity after the foreshock/mainshock sequence (Klyuchevskoy, Karymsky, Krasheninnikov, Kambalny, possibly Alaid and Ebeko), while others appear to have intervals of decreased activity (Sheveluch, Bezymianny, Avachinsky, Mutnovsky, Gorely).

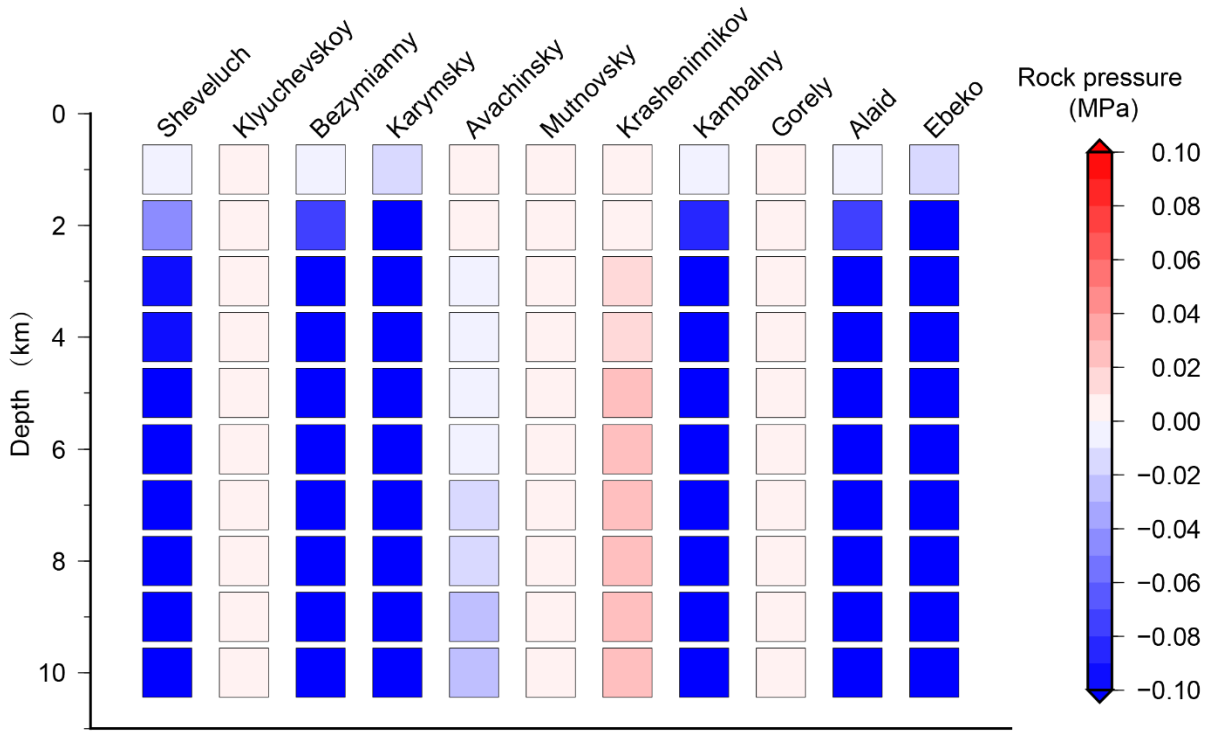

Fig. S27. Coseismic rock pressure at upper crustal depths caused by the 2025 M_W 8.8 earthquake for eleven volcanoes with time series shown in fig. S26.

Table 1. Comparison of Source Parameters of the 2025 M_W 8.8 Kamchatka Earthquake and the 2010 M_W 8.8 Maule Earthquake.

	2025 Kamchatka Earthquake (This study)	2010 Maule Earthquake (Yue et al., 2014)
M_0	2.26×10^{22} N·m	2.6×10^{22} N·m
E_r/M_0	0.37×10^{-5}	1.1×10^{-5}
Peak slip	~14 m	~17 m
Depth of peak slip	~22 km	~15 km
Rupture velocity	2.2 km/s	2.6 km/s
Rupture duration	270 s	120 s
Rupture length	~520 km	~560 km
Depth extension	10-60 km	10-60 km
Static stress drop	~10 MPa	~7 MPa

References and Notes

1. R. Herrendörfer, Y. Van Dinther, T. Gerya, L. A. Dalguer, Earthquake supercycle in subduction zones controlled by the width of the seismogenic zone. *Nat. Geosci.* **8**, 471–474 (2015).

2. G. P. Hayes, G. L. Moore, D. E. Portner, M. Hearne, H. Flamme, M. Furtney, G. M. Smoczyk, Slab2, a comprehensive subduction zone geometry model. *Science* **362**, 58–61 https://www.science.org/doi/10.1126/science.aat4723 (2018).

3. C. DeMets, R. G. Gordon, D. F. Argus, Geologically current plate motions. *Geophys. J. Int.* **181**, 1–80 (2010).

4. J. Kelleher, L. Sykes, J. Oliver, Possible criteria for predicting earthquake locations and their application to major plate boundaries of the Pacific and the Caribbean. *J. Geophys. Res.* **78**, 2547–2585 (1973).

5. V. M. Zobin, Apparent stress of earthquakes within the shallow subduction zone near Kamchatka Peninsula. *Bull. Seismol. Soc. Am.* **86**, 811–820 (1996).

6. O. J. Pérez, Kuril Islands Arc: Two seismic cycles of great earthquakes during which the complete history of seismicity ($Ms \geq 6$) is observed. *Bull. Seismol. Soc. Am.* **90**, 1096–1100 (2000).

7. V. K. Gusiakov, "Two Great Kamchatka Tsunamis, 1737 and 1952. IUGG Tsunami Commission" (Institute of Computational Mathematics and Mathematical Geophysics, Siberian Division, Russian Academy of Sciences, 2000); https://bibliotecadigital.ciren.cl/handle/20.500.13082/28986.

8. V. M. Zobin, V. I. Levina, The rupture process of the M_w 7.8 Cape Kronotsky, Kamchatka, earthquake of 5 December 1997 and its relationship to foreshocks and aftershocks. *Bull. Seismol. Soc. Am.* **91**, 1619–1628 (2001).

9. S. A. Fedotov, N. A. Dolbilkina, V. N. Morozov, V. I. Myachkin, V. B. Preobrazensky, G. A. Sobolev, Investigation on earthquake prediction in Kamchatka. *Tectonophysics* **9**, 249–258 (1970).

10. T. Rikitake, Recurrence of great earthquakes at subduction zones. *Tectonophysics* **35**, 335–362 (1976).

11. T. K. Pinegina, L. I. Bazanova, E. A. Zelenin, J. Bourgeois, A. I. Kozhurin, I. P. Medvedev, D. S. Vydrin, Holocene tsunamis in Avachinsky Bay, Kamchataka, Russia. *Pure Appl. Geophys.* **175**, 1485–1506 (2018).

12. T. K. Pinegina, J. Bourgeois, L. I. Bazanova, E. A. Zelenin, S. P. Krasheninnikov, M. V. Portnyagin, Coseismic coastal subsidence associated with unusually wide rupture of prehistoric earthquakes on the Kamchatka subduction zone: A record in buried erosional scarps and tsunami deposits. *Quat. Sci. Rev.* **233**, 106171 (2020).

13. M. Båth, H. Benioff, The aftershock sequence of the Kamchatka earthquake of November 4, 1952. *Bull. Seismol. Soc. Am.* **48**, 1–15 (1958).

14. A. Ben-Menahem, M. N. Toksöz, Source mechanism from spectrums of long-period surface waves: 2. The Kamchatka earthquake of November 4, 1952. *J. Geophys. Res.* **68**, 5207–5222 (1963).

15. H. Kanamori, Re-examination of the earth's free oxcillations excited by the Kamchatka earthquake of November 4, 1952. *Phys. Earth Planet. Inter.* **11**, 216–226 (1976).

16. J. M. Johnson, K. Satake, Asperity distribution of the 1952 great Kamchatka earthquake and its relation to future earthquake potential in Kamchatka. *Pure Appl. Geophys.* **154**, 541–553 (1999).

17. B. T. MacInnes, R. Weiss, J. Bourgeois, T. K. Pinegina, Slip distribution of the 1952 Kamchatka great earthquake based on near-field tsunami deposits and historical records. *Bull. Seismol. Soc. Am.* **100**, 1695–1709 (2010).

18. R. Bürgmann, M. G. Kogan, G. M. Steblov, G. Hilley, V. E. Levin, E. Apel, Interseismic coupling and asperity distribution along the Kamchatka subduction zone. *J. Geophys. Res.* **110**, 2005JB003648 (2005).

19. H. Benz, M. Herman, K. Furlong, E. Jones, R. Schmitt, W. Yeck, W. Barnhart, The 29 July 2025, *M* 8.8 Kamchatka Earthquake, U.S. Geological Survey StoryMap (USGS, 2025); https://earthquake.usgs.gov/storymap/index-kamchatka2025.html.

20. E. A. Okal, Use of the mantle magnitude M_m for the reassessment of the moment of historical earthquakes: I: Shallow events. *Pure Appl. Geophys.* **139**, 17–57 (1992).

21. National Geophysical Data Center/World Data Service, NCEI/WDS Global Historical Tsunami Database, NOAA National Centers for Environmental Information; https://doi.org/10.7289/V5PN93H7.

22. H. Kanamori, J. W. Given, Use of long-period surface waves for rapid determination of earthquake-source parameters. *Phys. Earth Planet. Inter.* **27**, 8–31 (1981).

23. NOAA PMEL Center for Tsunami Research, Kamchatka Tsunami, July 29, 2025 Main Event 436 Page, NOAA NCTR research product (NOAA, 2025); https://nctr.pmel.noaa.gov/kamchatka20250729.

24. E. E. Brodsky, T. Lay, Geophysics. Recognizing foreshocks from the 1 April 2014 Chile earthquake. *Science* **344**, 700–702 (2014).

25. M. Bouchon, V. Durand, D. Marsan, H. Karabulut, J. Schmittbuhl, The long precursory phase of most large interplate earthquakes. *Nat. Geosci.* **6**, 299–302 (2013).

26. A. N. Besedina, E. V. Novikova, P. V. Beloklokov, V. P. Komzeleva, E. A. Kulik, E. A. Marshakova, I. I. Nugmanov, K. Y. Potapova, Peculiarities of Localization Zones of the Major Earthquakes in the Kuril-Kamchatka Arc. *Izv. Russ. Acad. Sci., Phys. Solid Earth* **61**, 175–188 (2025).

27. L. Ye, T. Lay, H. Kanamori, The 25 March, 2020 M_w 7.5 Paramushir, northern Kuril Islands earthquake and major ($M_w \geq 7.0$) near-trench intraplate compressional faulting. *Earth Planet. Sci. Lett.* **556**, 116728 (2021).

28. C. H. Scholz, Earthquakes and friction laws. *Nature* **391**, 37–42 (1998).

29. T. Lay, H. Kanamori, C. J. Ammon, K. D. Koper, A. R. Hutko, L. Ye, T. M. Rushing, Depth-varying rupture properties of subduction zone megathrust faults. *J. Geophys. Res. Solid Earth* **117**, B04311 (2012).

30. A. Sladen, J. Trevisan, Shallow megathrust earthquake ruptures betrayed by their outer-trench aftershocks signature. *Earth Planet. Sci. Lett.* **483**, 105–113 (2018).

31. T. Lay, L. Ye, Z. Wu, H. Kanamori, Macrofracturing of oceanic lithosphere in complex large earthquake sequences. *J. Geophys. Res. Solid Earth* **125**, e2020JB020137 (2020).

32. H. Yue, T. Lay, L. Rivera, C. An, C. Vigny, X. Tong, J. C. Báez Soto, Localized fault slip to the trench in the 2010 Maule, Chile M_w = 8.8 earthquake from joint inversion of high-rate GPS, teleseismic body waves, InSAR, campaign GPS, and tsunami observations. *J. Geophys. Res. Solid Earth* **119**, 7786–7804 (2014).

33. K. F. Cheung, T. Lay, L. Sun, Y. Yamazaki, Tsunami size variability with rupture depth. *Nat. Geosci.* **15**, 33–36 (2022).

34. H. Kanamori, E. E. Brodsky, The physics of earthquakes. *Phys. Today* **54**, 34–40 (2001).

35. A. A. Gusev, L. S. Shumilina, Recurrence of Kamchatka strong earthquakes on a scale of moment magnitudes. *Izvest. Phys. Solid Earth* **40**, 206–215 (2004).

36. C. Gaedicke, R. Freitag, U. Barckhausen, D. Franke, S. Ladage, M. Schnabel, N. Tsukanov, "Subducting fracture zones control earthquake distribution and upper plate properties: Examples from Sumatra and Kamchatka", in *AGU Fall Meeting Abstracts* (AGU, 2010), vol. 2010, pp. T11D–2123.

37. C. Goldfinger, Y. Ikeda, R. S. Yeats, J. Ren, Superquakes and supercycles. *Seismol. Res. Lett.* **84**, 24–32 (2013).

38. B. Philibosian, K. Sieh, J. P. Avouac, D. H. Natawidjaja, H. W. Chiang, C. C. Wu, H. Perfettini, C.-C. Shen, M. R. Daryono, B. W. Suwargadi, Rupture and variable coupling behavior of the Mentawai segment of the Sunda megathrust during the supercycle culmination of 1797 to 1833. *J. Geophys. Res. Solid Earth* **119**, 7258–7287 (2014).

39. J. M. Nocquet, P. Jarrin, M. Vallée, P. A. Mothes, R. Grandin, F. Rolandone, B. Delouis, H. Yepes, Y. Font, D. Fuentes, M. Régnier, A. Laurendeau, D. Cisneros, S. Hernandez, A. Sladen, J.-C. Singaucho, H. Mora, J. Gomez, L. Montes, P. Charvis, Supercycle at the Ecuadorian subduction zone revealed after the 2016 Pedernales earthquake. *Nat. Geosci.* **10**, 145–149 (2017).

40. E. A. Wirth, V. J. Sahakian, L. M. Wallace, D. Melnick, The occurrence and hazards of great subduction zone earthquakes. *Nat. Rev. Earth Environ.* **3**, 125–140 (2022).

41. S. Ruiz, M. Moreno, D. Melnick, F. Del Campo, P. Poli, J. C. Báez, F. Leyton, R. Madariaga, Reawakening of large earthquakes in south central Chile: The 2016 M_w 7.6 Chiloé event. *Geophys. Res. Lett.* **44**, 6633–6640 (2017).

42. A. Y. Ozerov, O. A. Girina, N. A. Zharinov, A. B. Belousov, Y. V. Demyanchuk, Eruptions in the Northern Group of Volcanoes, in Kamchatka, during the early 21st century. *J. Volcanol. Seismol.* **14**, 1–17 (2020).

43. D. P. Hill, F. Pollitz, C. Newhall, Earthquake-volcano interactions. *Phys. Today* **55**, 41–47 (2002).

44. M. Manga, E. E. Brodsky, Seismic triggering of eruptions in the far field: Volcanoes and geysers. *Annu. Rev. Earth Planet. Sci.* **34**, 263–291 (2006).

45. T. R. Walter, F. Amelung, Volcanic eruptions following $M \geq 9$ megathrust earthquakes: Implications for the Sumatra-Andaman volcanoes. *Geology* **35**, 539–542 (2007).

46. G. Seropian, B. M. Kennedy, T. R. Walter, M. Ichihara, A. D. Jolly, A review framework of how earthquakes trigger volcanic eruptions. *Nat. Commun.* **12**, 1004 (2021).

47. O. A. Girina, N. V. Gorbach, V. O. Davydova, D. V. Melnikov, T. M. Manevich, A. G. Manevich, Y. V. Demyanchuk, The 15 March, 2019 Bezymianny Volcano explosive eruption and its products. *J. Volcanol. Seismol.* **14**, 394–409 (2020).

48. S. Eggert, T. R. Walter, Volcanic activity before and after large tectonic earthquakes: Observations and statistical significance. *Tectonophysics* **471**, 14–26 (2009).

49. T. Nishimura, Triggering of volcanic eruptions by large earthquakes. *Geophys. Res. Lett.* **44**, 7750–7756 (2017).

50. L. Caricchi, M. Townsend, E. Rivalta, A. Namiki, The build-up and triggers of volcanic eruptions. *Nat. Rev. Earth Environ.* **2**, 458–476 (2021).

51. I. Koulakov, I. Abkadyrov, N. Al Arifi, E. Deev, S. Droznina, E. I. Gordeev, A. Jakovlev, S. El Khrepy, R. I. Kulakov, Y. Kugaenko, A. Novgorodova, S. Senyukov, N. Shapiro, T. Stupina, M. West, Three different types of plumbing system beneath the neighboring active volcanoes of Tolbachik, Bezymianny, and Klyuchevskoy in Kamchatka. *J. Geophys. Res. Solid Earth* **122**, 3852–3874 (2017).

52. I. Koulakov, P. Plechov, R. Mania, T. R. Walter, S. Z. Smirnov, I. Abkadyrov, A. Jakovlev, V. Davydova, S. Senyukov, N. Bushenkova, A. Novgorodova, T. Stupina, S. Y. Droznina, Anatomy of the Bezymianny volcano merely before an explosive eruption on 20.12.2017. *Sci. Rep.* **11**, 1758 (2021).

53. B. L. N. Kennett, E. R. Engdahl, Traveltimes for global earthquake location and phase identification. *Geophys. J. Int.* **105**, 429–465 (1991).

54. C. Liu, T. Lay, Z. Xie, X. Xiong, Intraslab deformation in the 30 November 2018 Anchorage, Alaska, M_w 7.1 earthquake. *Geophys. Res. Lett.* **46**, 2449–2457 (2019).

55. U. Wegnüller, C. Werner, T. Strozzi, A. Wiesmann, O. Frey, M. Santoro, Sentinel-1 support in the GAMMA software. *Procedia Comput. Sci.* **100**, 1305–1312 (2016).

56. T. G. Farr, P. A. Rosen, E. Caro, R. Crippen, R. Duren, S. Hensley, M. Kobrick, M. Paller, E. Rodriguez, L. Roth, D. Seal, S. Shaffer, J. Shimada, J. Umland, M. Werner, M. Oskin, D. Burbank, D. Alsdorf, The shuttle radar topography mission. *Rev. Geophys.* **45**, 2005RG000183 (2007).

57. C. Yu, Z. Li, N. T. Penna, P. Crippa, Generic atmospheric correction model for interferometric synthetic aperture radar observations. *J. Geophys. Res. Solid Earth* **123**, 9202–9222 (2018).

58. C. Ji, D. J. Wald, D. V. Helmberger, Source description of the 1999 Hector Mine, California, earthquake, part I: Wavelet domain inversion theory and resolution analysis. *Bull. Seismol. Soc. Am.* **92**, 1192–1207 (2002).

59. C. Ji, D. V. Helmberger, D. J. Wald, K. F. Ma, Slip history and dynamic implications of the 1999 Chi-Chi, Taiwan, earthquake. *J. Geophys. Res.* **108**, 2002JB001764 (2003).

60. G. Laske, G. Masters, Z. Ma, M. Pasyanos, Update on CRUST1. 0-A 1-degree global model of Earth's crust. *Geophys. Res. Abstr.* **15**, 2658 (2013).

61. C. A. Langston, D. V. Helmberger, A procedure for modelling shallow dislocation sources. *Geophys. J. R. Astron. Soc.* **42**, 117–130 (1975).

62. F. Dahlen, J. Tromp, *Theoretical Global Seismology* (Princeton Univ. Press, 1999).

63. Y. Bai, C. Liu, T. Lay, K. F. Cheung, L. Ye, Optimizing a model of coseismic rupture for the 22 July 2020 M_w 7.8 Simeonof earthquake by exploiting acute sensitivity of tsunami excitation across the shelf break. *J. Geophys. Res. Solid Earth* **127**, e2022JB024484 (2022).

64. C. Liu, Y. Bai, T. Lay, Y. Feng, X. Xiong, Megathrust complexity and the up-dip extent of slip during the 2021 Chignik, Alaska Peninsula earthquake. *Tectonophysics* **854**, 229808 (2023).

65. C. Liu, Y. Zheng, X. Xiong, R. Wang, A. López, J. Li, Rupture processes of the 2012 September 5 M_w 7.6 Nicoya, Costa Rica earthquake constrained by improved geodetic and seismological observations. *Geophys. J. Int.* **203**, 175–183 (2015).

66. Y. Yamazaki, Z. Kowalik, K. F. Cheung, Depth-integrated, non-hydrostatic model with grid nesting for tsunami generation, propagation, and run-up. *Int. J. Numer. Methods Fluids* **67**, 2081–2107 (2009).

67. Y. Bai, K. F. Cheung, Dispersion and nonlinearity of multi-layer non-hydrostatic free-surface flow. *J. Fluid Mech.* **726**, 226–260 (2013).

68. Y. Bai, K. F. Cheung, Linear shoaling of free-surface waves in multi-layer non-hydrostatic models. *Ocean Model.* **121**, 90–104 (2018a).

69. X. Wei, H. Zhi, Y. Bai, Multi-layer non-hydrostatic free-surface flow model with kinematic seafloor for seismic tsunami generation. *Coast. Eng.* **193**, 104580 (2024).

70. Y. Bai, K. F. Cheung, Dispersion and kinematics of multi-layer non-hydrostatic models. *Ocean Model.* **92**, 11–27 (2015a).

71. Y. Bai, Y. Yamazaki, K. F. Cheung, Interconnection of multi-scale standing waves across the Pacific Basin from the 2011 Tohoku tsunami. *Ocean Model.* **92**, 183–197 (2015b).

72. Y. Bai, Y. Yamazaki, K. F. Cheung, Amplification of drawdown and runup over Hawaii's insular shelves by tsunami N-waves from mega Aleutian earthquakes. *Ocean Model.* **124**, 61–74 (2018b).

73. Y. Bai, Y. Yamazaki, K. F. Cheung, Convergence of multilayer nonhydrostatic models in relation to Boussinesq-type equations. *J. Waterw. Port Coast. Ocean Eng.* **144**, 06018001 (2018c).

74. Y. Bai, Y. Yamazaki, K. F. Cheung, Intercomparison of hydrostatic and nonhydrostatic modeling for tsunami inundation mapping. *Phys. Fluids* **35**, 077111 (2023b).

75. Y. Yamazaki, K. F. Cheung, Z. Kowalik, Depth-integrated, non-hydrostatic model for wave breaking and run-up. *Int. J. Numer. Methods Fluids* **61**, 473–497 (2011).

76. Y. Yamazaki, Y. Bai, L. L. Goo, K. F. Cheung, T. Lay, Nonhydrostatic modeling of tsunamis from earthquake rupture to coastal impact. *J. Hydraul. Eng. (N.Y.)* **149**, 04023033 (2023).

77. T. Lay, L. Ye, Y. Bai, K. F. Cheung, H. Kanamori, The 2018 M_w 7.9 Gulf of Alaska earthquake: Multiple fault rupture in the Pacific plate. *Geophys. Res. Lett.* **45**, 9542–9551 (2018).

78. L. Ye, Y. Bai, D. Si, T. Lay, K. F. Cheung, H. Kanamori, Rupture model for the 29 July 2021 M_w 8.2 Chignik, Alaska earthquake constrained by seismic, geodetic, and tsunami observations. *J. Geophys. Res. Solid Earth* **127**, e2021JB023676 (2022).

79. Y. Bai, C. Liu, T. Lay, K. F. Cheung, Y. Yamazaki, Fast and slow intraplate ruptures during the 19 October 2020 magnitude 7.6 Shumagin earthquake. *Nat. Commun.* **14**, 2015 (2023b).

80. C. Liu, Y. Bai, T. Lay, P. He, Y. Wen, X. Wei, X. Xiong, X. Xiong, Shallow crustal rupture in a major M_w 7.5 earthquake above a deep crustal seismic swarm along the Noto Peninsula in western Japan. *Earth Planet. Sci. Lett.* **648**, 119107 (2024).

81. Y. Yamazaki, K. F. Cheung, T. Lay, S. M. La Selle, R. C. Witter, B. E. Jaffe, A 700-year rupture sequence of great eastern Aleutian earthquakes from tsunami modeling of stratigraphic records. *Nat. Commun.* **16**, 2638 (2025).

82. Y. Okada, Surface deformation due to shear and tensile faults in a half-space. *Bull. Seismol. Soc. Am.* **75**, 1135–1154 (1985).

83. Y. Tanioka, K. Satake, Tsunami generation by horizontal displacement of ocean bottom. *Geophys. Res. Lett.* **23**, 861–864 (1996).

84. C. H. Scholz, *The Mechanics of Earthquakes and Faulting* (Cambridge Univ. Press, ed. 3, 2019).

85. R. Wang, F. Lorenzo-Martín, F. Roth, PSGRN/PSCMP-a new code for calculating co-and post-seismic deformation, geoid and gravity changes based on the viscoelastic-gravitational dislocation theory. *Comput. Geosci.* **32**, 527–541 (2006).

86. J. Ripperger, P. M. Mai, Fast computation of static stress changes on 2D faults from final slip distributions. *Geophys. Res. Lett.* **31**, 2004GL020594 (2004).

87. C. Liu, Simple unilateral rupture of the great Mw 8.8 2025 Kamchatka earthquake. Zenodo (2026); https://doi.org/10.5281/zenodo.18466362.